PAPER • OPEN ACCESS

Unconventional edge states in a two-leg ladder

To cite this article: C A Downing *et al* 2024 *New J. Phys.* **26** 073014

IOP Publishing New J. Phys. 26 (2024) 073014 https://doi.org/10.1088/1367-2630/ad5bf9

New Journal of Physics
The open access journal at the forefront of physics

Deutsche Physikalische Gesellschaft DPG
IOP Institute of Physics

Published in partnership with: Deutsche Physikalische Gesellschaft and the Institute of Physics

OPEN ACCESS

RECEIVED
5 February 2024

REVISED
8 June 2024

ACCEPTED FOR PUBLICATION
25 June 2024

PUBLISHED
8 July 2024

PAPER

Unconventional edge states in a two-leg ladder

C A Downing[1,*], L Martín-Moreno[2,3] and O I R Fox[1]

[1] Department of Physics and Astronomy, University of Exeter, Exeter EX4 4QL, United Kingdom
[2] Instituto de Nanociencia y Materiales de Aragón (INMA), CSIC-Universidad de Zaragoza, 50009 Zaragoza, Spain
[3] Departamento de Física de la Materia Condensada, Universidad de Zaragoza, 50009 Zaragoza, Spain
[*] Author to whom any correspondence should be addressed.

E-mail: c.a.downing@exeter.ac.uk

Keywords: edge states, tight-binding model, bulk-edge correspondence, two-leg ladder, participation ratio, energy level statistics, localization

Abstract

Some popular mechanisms for restricting the diffusion of waves include introducing disorder (to provoke Anderson localization) and engineering topologically non-trivial phases (to allow for topological edge states to form). However, other methods for inducing somewhat localized states in elementary lattice models have been historically much less studied. Here we show how edge states can emerge within a simple two-leg ladder of coupled harmonic oscillators, where it is important to include interactions beyond those at the nearest neighbor range. Remarkably, depending upon the interplay between the coupling strength along the rungs of the ladder and the next-nearest neighbor coupling strength along one side of the ladder, edge states can indeed appear at particular energies. In a wonderful manifestation of a type of bulk-edge correspondence, these edge state energies correspond to the quantum number for which additional stationary points appear in the continuum bandstructure of the equivalent problem studied with periodic boundary conditions. Our theoretical results are relevant to a swathe of classical or quantum lattice model simulators, such that the proposed edge states may be useful for applications including waveguiding in metamaterials and quantum transport.

1. Introduction

The theory of the localization of electrons due to disorder, as created by randomness in the atomic lattice, is a towering achievement in condensed matter physics [1, 2]. This phenomena of an absence of diffusion can be observed throughout waves physics, including in acoustics, electromagnetics and photonics [3, 4]. Localization in perfectly ordered systems is also possible, most famously thanks to Wannier–Stark localization whereby an applied electric field breaks the periodicity of the lattice [5, 6]. Latterly, the rise of topological matter has celebrated the presence of highly localized states hosted by certain lattices, including topologically-protected edge states which exist in the gaps formed between bands filled with extended states [7–9]. Furthermore and perhaps counterintuitively, the reality of so-called bound states in the continuum—in the broadest sense, localized states existing within a continuous spectrum of delocalized waves—have also been demonstrated in a series of photonic architectures [10–13] nearly a century after the original idea of von Neumann and Wigner [14].

Within condensed matter theory, the consideration of couplings going beyond the nearest-neighbor approximation is a perennially popular activity within standard treatments of lattice models [15–19]. Laterly, spiritually similar theoretical studies have been performed for acoustical, optical, and phononic platforms amongst others, with interesting implications for topological phases and for the creation of rather exotic dispersion relations [20–26]. Experimentally, physical systems with non-negligible interactions beyond those of the nearest-neighbor type have been reliably produced, in some cases with tunability, using atomic spins inside a cavity [27]; acoustic metamaterials [28]; elastic metamaterials [29–31]; coupled optical cavities [32, 33], and exciton-polariton condensates in microcavities [34, 35]. However, thus far the creation of edge states

due to the inclusion of longer-range coupling has been mostly ignored, perhaps because of the seemingly contradictory concepts at play.

Here we propose exploiting longer-range couplings in order to generate edge states—without recourse to disorder, aperiodicity or topological non-trivialities. As a prototypical system, we employ a bosonic two-leg ladder model [36–41], which has already been explored experimentally to great effect using ultracold atoms for example [42–47]. While previous studies of so-called 'biased' two-leg ladders have considered either interchain energy detunings across the two legs of the ladder or different two-body onsite interaction terms [48–51], here we consider a bias in the range of the couplings themselves. We suppose that the two-leg ladder is composed of an upper chain A (marked in pink in figure 1(a)) which exhibits both nearest-nearest and next-nearest-neighbor couplings, and a lower chain B (depicted in yellow in panel (a)) which only sustains nearest-neighbor interactions. Perhaps surprisingly, this coupling imbalance raises the possibility for edge states to emerge amongst the expected plethora of extended states which are spread throughout the ordered lattice, as implied in the probability density plots already previewed in figures 1(b) and (c). Notably, the next-nearest-neighbor coupling introduces additional stationary points in the bandstructure (found in the continuum limit, after employing periodic boundary conditions) which occur for a certain quantum number q, which is associated with a definite eigenfrequency [52]. This particular bandstructure eigenfrequency is in turn exactly the energy of the edge state (found after diagonalization of the analogous finite-sized lattice problem with the implied open boundary conditions), which suggests a sort of bulk-edge correspondence between the generation of auxiliary stationary points and the appearance of edge states. Furthermore, the discovered edge states appear inside the notional band of extended states, such they may be thought of as a kind of bound state in the continuum, a flavor of state which is of a high current interest within modern condensed matter physics [10–13].

The Hamiltonian operator $\hat{H}$ of the bosonic two-leg ladder sketched in figure 1(a) is composed of just three parts

$$\hat{H} = \hat{H}_A + \hat{H}_B + \hat{H}_{A-B}, \tag{1}$$

where $\hat{H}_A$ describes the N coupled harmonic oscillators comprising the chain A subsystem (depicted as pink spheres in figure 1(a)) via the following Hamiltonian (we have set $\hbar = 1$ here and throughout)

$$\hat{H}_A = \sum_{n=1}^{N} \omega_0 a_n^\dagger a_n + \sum_{n=1}^{N-1} J_1 \left(a_{n+1}^\dagger a_n + a_n^\dagger a_{n+1} \right) + \sum_{n=1}^{N-2} J_2 \left(a_{n+2}^\dagger a_n + a_n^\dagger a_{n+2} \right). \tag{2}$$

The nearest-neighbor coupling strength $J_1 > 0$ (red arrow in figure 1(a)), and the next-nearest-neighbor coupling strength J_2 (cyan arrow) satisfies the inequality $0 \leqslant J_2 \leqslant J_1$. The N oscillators in the chain B subsystem (yellow spheres in figure 1(a)), on the opposite side of the rung to their chain A counterparts, are governed by a standard nearest-neighbor tight-binding Hamiltonian $\hat{H}_B$, where

$$\hat{H}_B = \sum_{n=1}^{N} \omega_0 b_n^\dagger b_n + \sum_{n=1}^{N-1} J_1 \left(b_{n+1}^\dagger b_n + b_n^\dagger b_{n+1} \right). \tag{3}$$

The creation and annihilation operators $c_n^\dagger$ and c_n create and destroy a bosonic excitation on the nth rung of the ladder, where the two possible flavors of operator $c_n = \{a_n, b_n\}$ refer to the site at the top or bottom of the nth rung, and where the bosonic commutation relation $[c_n, c_n^\dagger] = 1$ is always observed. The common resonance frequency of all $2N$ oscillators throughout the two-leg ladder is ω_0, although all of our results can easily be generalized to the case when the upper chain and lower chain have different resonance frequencies (this situation is briefly discussed later on in an appendix). Each oscillator is coupled to its adjacent partner along the rung (of the opposite flavor, A or B) via the coupling Hamiltonian

$$\hat{H}_{A-B} = \sum_{n=1}^{N} g \left(a_n^\dagger b_n + b_n^\dagger a_n \right). \tag{4}$$

The inter-chain coupling strength $g > 0$ (purple arrow in figure 1(a)), such that the two dimensionless parameters of primary interest for the full model of equation (1) are the next-nearest neighbor coupling ratio J_2/J_1, with a size between $0 \leqslant J_2/J_1 \leqslant 1$, and the inter-chain coupling ratio $g/J_1 \geqslant 0$. Together these coupling ratios control two important aspects of the overall model. Increasing J_2/J_1 allows for more stationary points in the continuum Hamiltonian bandstructure to emerge [52], which raises the possibility for interference effects. For example, the group velocity and phase velocity may be in the same direction for one mode and in the opposite direction for another mode somewhere elsewhere in the Brillouin zone [22]. Meanwhile,

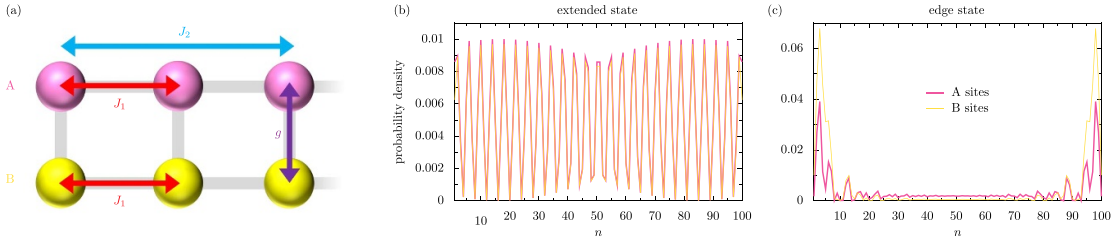

Figure 1. Unconventional edge states in the bosonic two-leg ladder model. Panel (a): a sketch of the two-leg ladder system under consideration, composed of two linear chains (denoted A and B) of quantum harmonic oscillators. Each oscillator is coupled (with the strength g, purple arrows) to its partner across the rung. The upper chain (A, pink balls) exhibits both nearest-neighbor coupling (with the strength J_1, red arrows) and next-nearest-neighbor coupling (with the strength J_2, cyan arrows). The lower chain (B, yellow balls) displays nearest-neighbor coupling (with J_1, red arrows) only. The rungs are equally spaced at intervals of the distance d along the ladder. Panel (b): the probability density of a typical extended state over the $2N$ sites of the two-leg ladder. The results for the A and B sites n are shown with pink and yellow lines respectively. Panel (c): the equivalent profile of a typical edge state. In the figure, we consider a two-leg ladder with a total of $2N = 200$ oscillators, and the couplings $g = 3J_1/2$ and $J_2 = J_1$. The scaled participation ratio $\mathrm{PR}(m)/2N$ of the states considered is the rather typical $\simeq$0.675 in panel (b) and perhaps surprisingly just $\simeq$0.171 in panel (c).

increasing g/J_1 allows for more mixing between the chain A and chain B subsystems which, due to their different boundary conditions coming from their different coupling ranges, raises the possibility for novel states to be forged in the combined ladder system.

In what follows, we discuss the band theory of the total Hamiltonian $\hat{H}$ of equation (1) in the infinitely long limit (and with periodic boundary conditions) in section 2, which hints at novel states near to additional stationary points which arise due to interactions beyond nearest-neighbor when the coupling strength $J_1/4 \leqslant J_2 \leqslant J_1$. We consider the proper finite system defined by equation (1) in section 3 (with its implied open boundary conditions), where we quantify the degree of localization of the eigenstates using the participation ratio. We also judge the character of the eigenvalue statistics using the mean value of the consecutive energy level spacings, which allows us to paint the extended state-to-edge state phase diagram of the model in figure 3. Some conclusions from our theoretical study are drawn in section 4. We relegate to the appendices a complete treatment of the chain A subsystem model in the appendix A, including a derivation of the analytic form of the density of states beyond nearest neighbor interactions, and an analysis of the chain B subsystem model in appendix B, including a derivation of the analytic probability density function associated with the adjacent energy level spacings. Finally, some supplementary results for the full two-leg ladder are housed within appendix C, while appendix D briefly considers a small extension of that model to allow for interchain energy detunings.

2. Band theory

Let us start by considering the full two-leg ladder model in the limit of large system size ($N \to \infty$) and after employing periodic boundary conditions, which allows for an analytic treatment of the continuum theory. Our hope is for the continuum model to have some descriptive power over the finite-sized system, in a similar manner to how the so-called bulk-edge correspondence in the physics of topological matter suggests that a topological invariant can predict the presence or absence of topological edge states [8, 9]. We introduce the pair of exponential Fourier transforms for the bosonic operators a_n and b_n appearing in the ladder model of equation (1) as follows

$$a_n = \frac{1}{\sqrt{N}} \sum_q \mathrm{e}^{\mathrm{i}nqd} a_q, \qquad b_n = \frac{1}{\sqrt{N}} \sum_q \mathrm{e}^{\mathrm{i}nqd} b_q, \tag{5}$$

with the quantum number $q = 2\pi m/Nd$, where the integer $m \in [-N/2, +N/2]$ implies that the first Brillouin zone exists for $-\pi/d < q \leqslant \pi/d$. The length scale d enters equation (5) due to the periodicity of the lattice, which repeats itself with identical rungs existing after every spacing d along the ladder (cf figure 1(a)). Substitution of equation (5) into the total Hamiltonian operator $\hat{H}$ of equation (1) leads to the q-space form of the Hamiltonian

$$\hat{H} = \sum_q \omega_q^A a_q^\dagger a_q + \sum_q \omega_q^B b_q^\dagger b_q + \sum_q g\left(a_q^\dagger b_q + b_q^\dagger a_q\right), \tag{6}$$

where the two eigenfrequencies ω_q^A and ω_q^B, which are associated with modes belonging to the individual chains A and B respectively, read

$$\omega_q^A = \omega_0 + 2J_1\cos(qd) + 2J_2\cos(2qd), \tag{7}$$

$$\omega_q^B = \omega_0 + 2J_1\cos(qd), \tag{8}$$

which immediately highlights an important coupling asymmetry amongst the two subsystems. Rearranging the transformed equation (6) into the neater form

$$\hat{H} = \sum_q \Psi_q^\dagger \mathcal{H}_q \Psi_q, \tag{9}$$

where the 2×2 Bloch Hamiltonian $\mathcal{H}_q$ and the column vector Ψ_q (which contains the relevant operators) are together defined by

$$\mathcal{H}_q = \begin{pmatrix} \omega_q^A & g \\ g & \omega_q^B \end{pmatrix}, \qquad \Psi_q = \begin{pmatrix} a_q \\ b_q \end{pmatrix}, \tag{10}$$

reveals some important properties of the model. Namely, the model respects only one of three important Bloch Hamiltonian symmetries (time-reversal, inversion and chiral) as follows

$$\mathcal{H}_q = \mathcal{H}_{-q}^*, \qquad \text{(time-reversal symmetry is observed)} \tag{11}$$

$$\mathcal{I}\mathcal{H}_q\mathcal{I}^{-1} \neq \mathcal{H}_{-q}, \qquad \text{(inversion symmetry is not observed)} \tag{12}$$

$$\mathcal{C}\mathcal{H}_q\mathcal{C}^{-1} \neq -\mathcal{H}_q, \qquad \text{(chiral symmetry is not observed)} \tag{13}$$

where the inversion operator $\mathcal{I} = \sigma_x$ and the chiral operator $\mathcal{C} = \sigma_z$. Both operators are given in terms of one of the three Pauli spin matrices $\boldsymbol{\sigma} = (\sigma_x, \sigma_y, \sigma_z)$, while I is the identity matrix. As usual, time-reversal symmetry is respected since no magnetic (or even pseudo-magnetic) field is present (cf equation (11)). Inversion symmetry is in general broken because as soon as the next-nearest-neighbor coupling $J_2 \neq 0$, then the diagonal terms in the Bloch Hamiltonian $\mathcal{H}_q$ are unequal ($\omega_q^A \neq \omega_q^B$), such that the system is indeed altered upon interchanging type A oscillators with type B oscillators throughout the ladder (cf equation (12)). Chiral (or sublattice) symmetry is not obeyed due to the nonzero couplings terms $J_1 \neq 0$ and $J_2 \neq 0$ in the on-diagonal terms of the Bloch Hamiltonian $\mathcal{H}_q$, which ensure that the spectrum is not symmetric about ω_0 (the trivial breaking of chiral symmetry by the constant energy term ω_0, appearing in both ω_q^A and ω_q^B, is not consequential as it is just an arbitrary energy shift) (cf equation (13)). This brief symmetry analysis suggests that the proposed model likely cannot be classified with a traditional topological index as per the Altland–Zirnbauer table [53, 54], such that any edge states arising in the two-leg ladder should probably be deemed to be topologically trivial. Indeed, the winding number suggested by the curve formed in a parametric plot of the Bloch Hamiltonian $\mathcal{H}_q = \mathcal{H}_I I + \boldsymbol{\sigma}\cdot\boldsymbol{\mathcal{H}}$ over the first Brillouin zone is zero. Here the three-dimensional Hamiltonian vector $\boldsymbol{\mathcal{H}} = (\mathcal{H}_x, \mathcal{H}_y, \mathcal{H}_z)$, and the employed Pauli matrix decomposition implies that the on-diagonal term $\mathcal{H}_I = \omega_0 + 2J_1\cos(qd) + J_2\cos(2qd)$, the off-diagonal term $\mathcal{H}_x = g$ is a constant, the leading diagonal imbalance term $\mathcal{H}_z = J_2\cos(2qd)$, and finally $\mathcal{H}_y = 0$.

The eigenvalues of the Bloch Hamiltonian $\mathcal{H}_q$ (cf equation (10)) suggest the pair of eigenfrequencies $\omega_{q,\tau}$ of the two-leg ladder, which are grouped into two bands (as codified by the index $\tau = \pm 1$) as follows

$$\omega_{q,\tau} = \bar{\omega}_q + \tau\Omega_q. \tag{14}$$

The expression of equation (14) makes use of $\bar{\omega}_q$, the average eigenfrequency of the uncoupled chains A and B encompassing the ladder, and the effective coupling constant Ω_q, which are together defined by

$$\bar{\omega}_q = \frac{\omega_q^A + \omega_q^B}{2} = \omega_q^B + J_2\cos(2qd), \tag{15}$$

$$\Omega_q = \sqrt{\Delta_q^2 + g^2} = \sqrt{J_2^2\cos^2(2qd) + g^2}, \tag{16}$$

$$\Delta_q = \frac{\omega_q^A - \omega_q^B}{2} = J_2\cos(2qd), \tag{17}$$

where Δ_q is the detuning across the two subsystem chains A and B. The eigendecomposition of equation (10), aided by the eigenfrequencies $\omega_{q,\tau}$ of equation (14), directly leads to the diagonal form of the original two-leg ladder Hamiltonian operator $\hat{H}$ of equation (1) like so

$$\hat{H} = \sum_{q,\tau} \omega_{q,\tau}\beta_{q,\tau}^\dagger\beta_{q,\tau}, \tag{18}$$

where the twin Bogoliubov operators $\beta_{q,\tau}$ introduced above are defined by the operator superpositions

$$\beta_{q,+} = \sin\theta_q\, a_q - \cos\theta_q\, b_q, \qquad \beta_{q,-} = \cos\theta_q\, a_q + \sin\theta_q\, b_q, \tag{19}$$

with the two trigonometric Bogoliubov coefficients which have emerged are given by

$$\cos\theta_q = \tfrac{1}{\sqrt{2}}\left(1+\tfrac{\Delta_q}{\Omega_q}\right)^{\frac{1}{2}}, \qquad \sin\theta_q = \tfrac{1}{\sqrt{2}}\left(1-\tfrac{\Delta_q}{\Omega_q}\right)^{\frac{1}{2}}, \tag{20}$$

which are determinable from the two quantities Ω_q and Δ_q, as defined in equations (16) and (17) respectively. The knowledge of the eigenfrequencies and eigenstates of the two-leg ladder allows for some general properties of the system to be inferred within standard band theory, and we restrict our analysis to the first Brillouin zone $-\pi/d < q \leqslant \pi/d$ only due to the periodicity of the considered lattice geometry.

The group velocity $v_{q,\tau} = \partial_q \omega_{q,\tau}$ for a mode in the band $\tau = \pm 1$ and with the quantum number q, follows directly from equation (14) as

$$v_{q,\tau} = -2d\left[J_1 \sin(qd) + J_2 \sin(2qd)\right] - \tau \frac{J_2^2 d}{\Omega_q} \sin(4qd)\,. \tag{21}$$

Clearly there are always, that is for both bands $\tau = \pm 1$ and for any values of J_2/J_1 and g/J_1, roots of the group velocity $v_{q,\tau}$ for modes at the centre and edge of the Brillouin zone with the quantum numbers $q = 0$ and $q = \pi/d$ respectively. For larger coupling ratios J_2/J_1, these two guaranteed roots are joined by additional stationary points. For example, in the extreme limit of $g \gg J_2$ the group velocity $v_{q,\tau}$ reduces to the band index independent quantity $v_{q,\tau} = -2d\left[J_1 \sin(qd) + J_2 \sin(2qd)\right]$. Upon transforming the variable from qd to $z = \mathrm{e}^{\mathrm{i}qd}$, the roots of the group velocity can be then be found by solving the quartic equation $J_2 z^4 + J_1 z^3 - J_1 z - J_2 = 0$. The already known roots of $q = 0$ and $q = \pi/d$ correspond to the twin solutions of $z = \pm 1$, essentially reducing the problem to the effectively quadratic equation $(z+1)(z-1)(J_2 z^2 + J_1 z + J_2) = 0$. The final two roots are then found to be located at $z = -J_1/(2J_2) \pm \mathrm{i}\sqrt{1 - J_1^2/(2J_2)^2}$, or equivalently at $qd = \pm(\pi - \arctan\sqrt{(2J_2/J_1)^2 - 1})$. This brief analysis suggests additional stationary points only occur above a critical coupling ratio $J_2/J_1 > 1/2$, at least in the considered regime $g \gg J_2$. A similar calculation may be performed in the opposing limit of $g \ll J_2$, when the two subsystems effectively decouple, which reveals a different threshold coupling ratio of $J_2/J_1 > 1/4$ for additional stationary points to emerge (see appendix A for the derivation). These additional stationary points in the bandstructure are found out to be highly consequential for the emergence of edge states, as is discussed later on.

The bandgap $\delta\omega$, defined as the energy difference between the minimum of the upper band $\omega_{q,+}$ and the maximum of the lower band $\omega_{q,-}$ for any value of the quantum number q, is given by the intuitive formula

$$\delta\omega = \min\left\{\omega_{q,+}\right\} - \max\left\{\omega_{q,-}\right\}, \tag{22}$$

which may be positive, negative or zero in the case of the considered ladder model. In particular, a negative bandgap $\delta\omega$ suggests band overlap since the lower band will necessarily protrude into the territory of the nominally upper band. In the simplest case of very weak next-nearest neighbor coupling $J_2 \ll J_1$, a negative bandgap only exists when the inequality $g < 2J_1$ holds, since $\min\{\omega_{q,+}\} = \omega_0 - 2J_1 + g$ and $\max\{\omega_{q,-}\} = \omega_0 + 2J_1 - g$ in this limit, such that the bandgap of equation (22) becomes $\delta\omega = 2(g - 2J_1)$ within this simple regime. The influence of the bandgap $\delta\omega$ on the appearance of edge states is discussed in detail in the next section.

We present graphically some visualizations of a few key results coming from the bandstructure of the two-leg ladder in the first two columns of figure 2, for the example case with the inter-chain coupling $g = 3J_1/2$. The first column of panels (a), (d), (g), (j) and (m) in figure 2 display the group velocity $v_{q,\tau}$ in the first Brillouin zone using equation (21), where descending the column increases the next-nearest neighbor coupling strength J_2 (as marked on the left-hand side of figure 2). The results for the upper band $\tau = +1$ are denoted with magenta lines, while the lower $\tau = -1$ band are associated with cyan lines. As discussed after equation (21), the guaranteed stationary points at $q = 0$ and $q = \pi/d$ are joined by additional stationary points for the cases of larger next-nearest neighbor couplings J_2, as marked by pink circles and cyan circles in the relevant figures 2(g), (j) and (m), where $J_2 \geqslant J_1/2$. The second column of figure 2 shows the eigenfrequencies $\omega_{q,\tau}$ corresponding to the cases of the first column and forming the exact bandstructure of the two-leg ladder via equation (14). The dashed pink and cyan lines mark the extrema of each ($\tau = \pm 1$) band, which imply a series of negative bandgaps (cf equation (22)) within the chosen parameter regime. Importantly, the final three panels (h), (k) and (n) in figure 2 contain pink circles and cyan circles in the same manner as the group velocity panels (g), (j) and (m), which correspond to stationary points in the bandstructure. In particular, the solid blue lines in panels (k) and (n) mark the frequencies $\omega_{q,\tau}$ of the modes

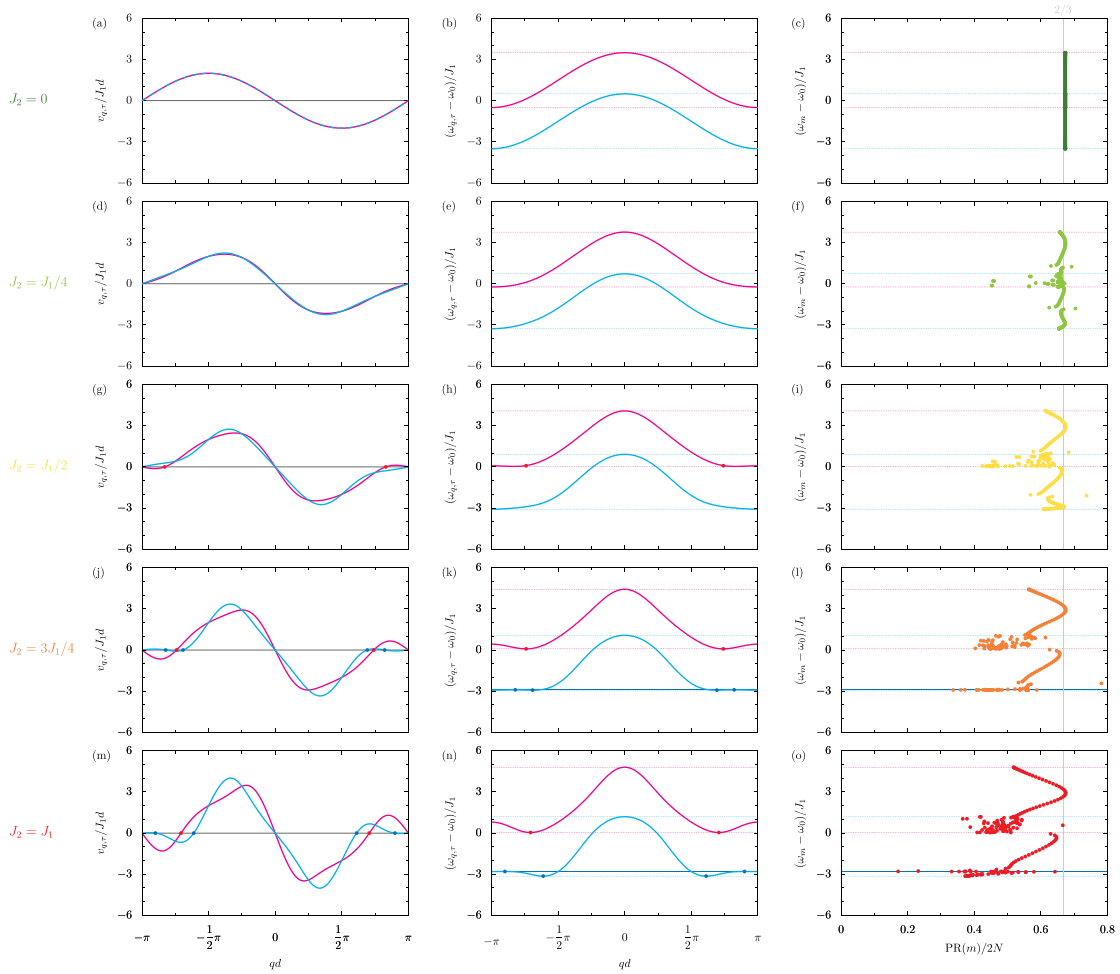

Figure 2. Stationary points, bandstructure and degrees of localization in the two-leg ladder model. We consider five increasingly large values of the next-nearest neighbor coupling J_2 upon descending the columns of the figure (as marked on the left-hand side), and we set the inter-chain coupling $g = 3J_1/2$. First column: the group velocity $v_{q,\tau}$ as a function of the quantum number q, in the first Brillouin zone $-\pi/d < q \leqslant \pi/d$. The results for the $\tau = +1$ (cyan lines) and $\tau = -1$ (pink lines) bands are shown. The calculation is carried out with periodic boundary conditions for a two-leg ladder in the limit of $2N \to \infty$ oscillators (cf equation (21)). In panels (g), (j) and (m), the significant J_2 couplings have given rise to extra roots in the group velocity (marked by pink and cyan circles), corresponding to additional stationary points in the bandstructure $\omega_{q,\tau}$, which are similarly marked in panels (h), (k) and (n). Second column: the eigenfrequencies $\omega_{q,\tau}$ forming the periodic bandstructure (cf equation (14)) and corresponding to the results of the first column. Dashed pink and cyan horizontal lines: the extrema of each ($\tau = \pm 1$) band, which are similarly carried through to the third column, and which imply a series of negative bandgaps (cf equation (22)). Solid blue horizontal lines in panels (k) and (n): the modes associated with additional stationary points in the lower $\tau = -1$ band, which are carried through to panels (l) and (o) in the third column. Third column: the scaled participation ratio PR$(m)/2N$ of each state m (cf equation (23)), which reside at the eigenfrequency ω_m. Solid grey verticle lines: guide for the eye at $2/3$. The numerical calculation in the third column is carried out with open boundary conditions for a two-leg ladder with $2N = 200$ oscillators.

which are associated with additional stationary points in the lower $\tau = -1$ band, which lies inside the energetic sector created by the upper and lower bounds of the lower $\tau = -1$ band (as denoted by the two dashed cyan lines). As such, if these modes are edge states, and if they are surrounded by a collection of extended states comprising the rest of the effective band, the highlighted modes will in essence be a type of bound state in the continuum [10–13]. In the next section 3, we finally consider the proper finite-sized two-leg ladder system as defined by equation (1), which allows us to probe the existence of edge states within the lattice model and their relation to certain bulk properties.

3. Finite-sized systems

Let us now consider the two-leg ladder Hamiltonian $\hat{H}$ as originally introduced in equation (1) for a ladder of finite length N, such that there are $2N$ coupled oscillators in the overall system. Upon staying in real space (instead of moving into q-space using the transformation of equation (5)) the Hamiltonian matrix $\mathcal{H}$ will be of size $2N \times 2N$ (instead of the 2×2 Bloch Hamiltonian matrix $\mathcal{H}_q$ of equation (10), as found within q-space). The diagonalization of the finite square matrix $\mathcal{H}$ (with implied open boundary conditions) is

readily achieved, leading to $2N$ eigenfrequencies ω_m, where the integer index $m = \{1, 2, \ldots, 2N\}$. For each state labeled by m, the nth element of the associated eigenvector can be written as $c_n(m)$, and there will be $2N$ elements in total, corresponding to each site in the two-leg ladder. The knowledge of the eigenvectors allows for the spread of the state across the whole lattice to be quantified using a popular localization measure: the participation ratio $\mathrm{PR}(m)$ of a state m. This quantity may be defined via the formula [55, 56]

$$\mathrm{PR}(m) = \frac{\left(\sum_n |c_n(m)|^2\right)^2}{\sum_n |c_n(m)|^4}, \tag{23}$$

where the numerator is simply a normalization, while the denominator discriminates between states with different spatial extents. In the case of the two-leg ladder considered here, the sums in equation (23) are taken over the whole array $n = \{1, 2, \ldots, 2N\}$. A fully localized state is trapped on just one site n, so that $\mathrm{PR}(m_{\text{f. localized}}) = 1$. Conversely, a fully extended state will feel all $2N$ sites equally, such that its participation ratio will scale exactly with the system size as $\mathrm{PR}(m_{\text{f. extended}}) = 2N$. Otherwise, typical extended states will observe a linear with system size relationship like $\mathrm{PR}(m_{\text{extended}}) \simeq \beta(2N)$, where the prefactor β is some dimensionless number which is known exactly for certain simple cases (see [57, 58] for example, while appendix B contains a derivation of the common prefactor $\beta = 2/3$ for a single regular chain). Away from these common scenarios, that is those with participation ratios scaling like $(2N)^0$ or $(2N)^1$, states exhibiting the more peculiar expression $\mathrm{PR}(m) \simeq \beta(2N)^\alpha$ are of great interest. Here the exponent α satisfies the inequality $0 < \alpha < 1$, such that the state has a distinctly sublinear dependence on the overall system size $2N$. These unusual states are then arguably localized to some degree, depending upon the exact size of the key exponent α. In some contexts (including quasiperiodic models), these states are sometimes known as multifractal states, where α is related to the fractal dimension of the state [59–61].

We explore the various degrees of localization of the states supported in the two-leg ladder in the third column of figure 2. As in the first and second columns of figure 2, the inter-chain coupling remains at $g = 3J_1/2$ and going down the column of panels (c), (f), (i), (l) and (o) increases the next-nearest neighbor coupling J_2, but now we consider a finite-sized array of $2N = 200$ oscillators as described by equation (1). We plot in figure 2 (c), (f), (i), (l) and (o) the eigenfrequencies ω_m, where each state is labeled by the index m, as a function of its participation ratio $\mathrm{PR}(m)$ (cf equation (23)). The simplest case of zero next-nearest neighbor coupling ($J_2 = 0$) is displayed in figure 2(c), where the common participation ratio of $\mathrm{PR}(m) \simeq (2/3)(2N)$ for all states m is most apparent, signaling rather standard extended states (indeed, the prefactor of $\beta \simeq 2/3$ is obtained analytically in appendix B). In figures 2(f) and (i), where the next-nearest neighbor coupling J_2 is nonzero but still relatively small, there are fluctuations around the value of $2/3$ (a number marked with a solid grey vertical line throughout the third column) suggesting typical extended states but without the complete uniformity of panel (c). Notably especially in panel (i), where $J_2 = J_1/2$, two collections of states have started to accumulate around the band edges of the upper and lower band (as found from the continuum calculation, and as marked with the dashed magenta and cyan horizontal lines in each panel). The cases with the largest next-nearest neighbor coupling J_2 in the lowest two panels finally reveal the formation of significantly less extended states, with the smallest scaled participation ratio being $\min\{\mathrm{PR}(m)\}/2N \simeq 0.171$ in figure 2(o), where $J_2 = J_1$. This state of minimum participation ratio in panel (o) resides at a certain eigenfrequency ω_m, as marked by a solid blue line, which corresponds to an eigenfrequency $\omega_{q,\tau}$ coming from the continuum model. This particular eigenfrequency $\omega_{q,\tau}$ is shown in the adjacent panel (n) by the same solid blue line. The specific quantum number q associated with this particular eigenfrequency $\omega_{q,\tau}$ is distinguished by a blue circle in panel (n), since it is a stationary point (all additional stationary points are marked with circles in the first two columns of figure 2, as discussed after equation (21) and as confirmed in the group velocity plots given in panels (g), (j) and (m)). Notably, the most localized state in panel (o) is also seen to be housed inside the notional spectral band of extended states (limited by the dashed horizontal lines), a defining characteristic of a bound state in the continuum [10–13].

We visualize two characteristic states in the two-leg ladder in figures 1(b) and (c), where the couplings $g = 3J_1/2$ and $J_2 = J_1$, and we consider a system with $2N = 200$ oscillators (which matches the parameter situation in figure 2(o)). We plot the probability density over the $2N$ sites of the array, where the results for the A and B sites n are shown with pink and yellow lines respectively. Notably, the example extended state shown in in figure 1(b) feels around two-thirds of the array, its scaled participation ratio $\mathrm{PR}(m)/2N \simeq 0.675$ and its oscillatory structure is noticeably balanced across both subsystems chain A and chain B. In figure 1(c) we finally reveal the spatial structure of the more localized state discussed in figure 2(o), of scaled participation ratio $\mathrm{PR}(m)/2N \simeq 0.171$, which is seen to be a type of edge state due to its significant probability density at the ends of the ladder (across both chain A and chain B). The correspondence between the appearance of an edge state in the finite system and the emergence of additional stationary points in the continuum bandstructure is somewhat reminiscent of the celebrated bulk-edge correspondence in

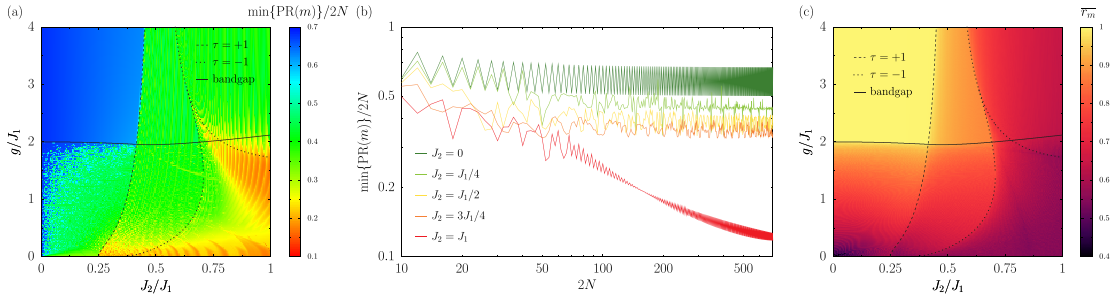

Figure 3. Degrees of localization and energy level statistics in the two-leg ladder model. Panel (a): a map of the minimum of the scaled participation ratio $\min\{\mathrm{PR}(m)\}/2N$, as a function of both the inter-chain coupling strength g and the next-nearest neighbor coupling strength J_2, both in units of the nearest-neighbor coupling J_1 (cf equation (23)). Dashed black line: boundary marking areas with different numbers of stationary points for the upper $\tau = +1$ band. Dotted black line: boundary marking areas with different numbers of stationary points for the lower $\tau = -1$ band. Solid black line: the borderline below which there is a negative bandgap. These indicative black lines are calculated from the continuum results of equations (14), (21) and (22). In this panel, we consider a two-leg ladder with $2N = 200$ oscillators. Panel (b): we take a horizontal cut through panel (a) at $g = 3J_1/2$, and then we make vertical cuts at five different values of J_2 (as noted in the plot legend), before extending the results as a function of the system size $2N$ in a log–log plot (up to $2N = 700$). Panel (c): a map of the mean consecutive energy level spacings $\overline{r_m}$, as a function of both g and J_2 (cf equation (27)). In this panel, we consider a two-leg ladder with $2N = 2000$ oscillators and the indicative black lines are the same as the lines provided in panel (a).

topological matter (where a calculation of a topological invariant from a continuum theory predicts the presence or absence of topological edge states in the finite version of the model [8, 9]).

We chart the degrees of localization of states supported by the two-leg ladder system more generally in figure 3. As a function of both the next-nearest neighbor coupling ratio J_2/J_1 and the inter-chain coupling ratio g/J_1, we plot the minimum of the scaled participation ratio $\min\{\mathrm{PR}(m)\}/2N$ in figure 3(a), where we consider a finite system again composed of $2N = 200$ oscillators. Blue and green regions in panel (a) represent cases where the ladder only supports highly extended states, which display the typical behavior of $\mathrm{PR}(m)/2N \sim 2/3$, while more interestingly the orange-red regions in the map suggest that the system may host somewhat localized states, since the localization measure $\mathrm{PR}(m)/2N \sim 1/10$. The map of figure 3(a) demonstrates the interplay between the key ratios J_2/J_1 and g/J_1: the next-nearest neighbor coupling ratio J_2/J_1 needs to be sufficiently large (in this case, $J_2 > J_1/4$) for a red phase to first appear, while if the inter-chain coupling ratio g/J_1 is too large (roughly, $g > 2J_1$) no red phase is supported. The general character of the diagram of figure 3(a) can be understood using some key results from the band theory of the continuum version of the model. Explicitly, as was discussed after equation (21) and also after equation (22), some limiting cases of the properties of the two-leg ladder with periodic boundary conditions suggest that

$$\text{additional stationary points arise when} \quad J_2 > \frac{J_1}{4}, \quad \text{for} \quad g \ll J_2, \tag{24}$$

$$\text{additional stationary points arise when} \quad J_2 > \frac{J_1}{2}, \quad \text{for} \quad g \gg J_2, \tag{25}$$

$$\text{a negative bandgap arises when} \quad g < 2J_1, \quad \text{for} \quad J_2 \ll J_1. \tag{26}$$

The inequality of equation (24) explains the critical behavior along the bottom horizontal axis of figure 3(a), as marked by the emergence of the red-orange colors, corresponding to the first appearance of stationary points due to next-nearest neighbor interactions. Meanwhile equation (25) is suggested at the top horizontal axis of figure 3(a), due to the transition from blue to green regions. The band overlap arising from a negative bandgap $\delta\omega$ arises when equation (26) is true, which actually approximately holds rather nicely for all of the range $0 \leqslant J_2 \leqslant J_1$. The solid black line in figure 3(a) demarcates the exact line in parameter space below which the bandgap $\delta\omega$ is negative (cf equation (22)). Similarly, the dashed black line marks areas with different numbers of stationary points for the upper band ($\tau = +1$), while the dotted black line does the same job for the lower band ($\tau = -1$). These three guides for the eye, arising from purely bulk calculations, certainly seem to coincide with interesting behavior of the corresponding finite system with edges. As an aside, when tending towards zero inter-chain coupling ($g \to 0$) we find a singular limit: just above the horizontal axis of figure 3(a) the red-orange colors when $J_2 > J_1/4$ refer to significantly smaller participation ratios, but this behavior is not found exactly at $g = 0$ (see for example the analyses of the individual chain A and chain B models in appendices A and B respectively). The occurrence of this singular limit lends some support to the notion that it is important for greater degrees of localization that the system contains subsystems with different boundary conditions, as here the upper and lower chain subsystems have

contrasting boundary conditions due to their different coupling ranges (which is only not relevant exactly when $g = 0$, as then the subsystems are completely decoupled).

A more accurate categorization of the nature of the extended states and edge states supported by the two-leg ladder requires an analysis which tracks changes due to size-dependencies. In figure 3(b) we effectively take a horizontal cut through panel (a) at the specific inter-chain coupling $g = 3J_1/2$, and then we make vertical cuts at five different values of J_2 (as noted in the plot legend). We then extending the result, the minimum of the scaled participation ratio $\min\{\mathrm{PR}(m)\}/2N$, as a function of the total number of oscillators in the ladder $2N$. This process results in the log-log plot presented as figure 3(b). Four of the lines in figure 3(b) effectively tend towards a constant (or oscillate between two constants in the case of the dark green line, where $J_2 = 0$) which suggests that the participation ratio scales linearly with $2N$: this data truly describes an extended phase of the system. However, the red line in figure 3(b), representing the case of $J_2 = J_1$, does not seem to tend towards a constant for the considered system sizes such that the participation ratio scales sublinearly with $2N$ (at least within this regime up to $2N = 700$). This suggests an unconventional phase containing edge states (cf the edge state depicted in figure 1(c) for the case of $2N = 200$ oscillators), albeit not fully localized states since the relationship is not completely independent of $2N$. Similar plots to figure 3(b) may be found in appendix C for other values of the specific inter-chain coupling g, providing further information about the overall phase diagram of figure 3(a). Notably, we draw our conclusions from these aforementioned finite size effect plots based upon system sizes from $\sim 10^1$ to $\sim 10^3$, since this regime can plausibly be explored experimentally [27–29]. We leave to a later study the numerical crunching of two-leg ladders containing larger numbers of oscillators, where the already-discovered non-monotonic nature of the data may revise some of the scalings between some ranges of exceedingly large $2N$ (in which case, the potential consequences will only effect the experimental study of extremely large systems). We also briefly discuss in appendix D the impact of a nonzero energy detuning between the resonance frequencies in the upper chain and lower chain as a complement to the data presented in figure 3, an analysis which also may be useful to guide certain future experiments and which hints at the possibility for inducing stronger degrees of localization thanks to energy detuning.

We further characterize the behavior of the two-leg ladder by considering the energy level statistics of the model [62, 63]. For a generic $2N \times 2N$ matrix Hamiltonian, we may list the resulting eigenvalues E_m in ascending order, where the index $m = \{1, 2, \ldots, 2N\}$. Therefore, there are $2N - 1$ consecutive energy level spacings S_m, where $S_m = E_{m+1} - E_m$. The ratio of two consecutive gaps r_m may then be defined as [64, 65]

$$r_m = \frac{\min\{S_m, S_{m-1}\}}{\max\{S_m, S_{m-1}\}}, \tag{27}$$

which observes the bounds $0 \leqslant r_m \leqslant 1$, where the index runs for $m = \{2, 3, \ldots, 2N - 1\}$. The dimensionless quantity r_m measures the correlations between the adjacent energy level gaps in a given spectrum. The mean value $\overline{r_m}$, found after averaging over all $2N - 1$ ratios r_m, acts as a kind of judge of the chaoticity appearing in the system. Some typical values of $\overline{r_m}$ for different categories of energy-level statistics are provided in [57, 65]: Poissonian level statistics are associated with $\overline{r_m} = 2\ln 2 - 1 \simeq 0.39$, while Gaussian orthogonal ensembles are characterized with $\overline{r_m} = 4 - 2\sqrt{3} \simeq 0.54$. In ordered (picket fence-like) models $\overline{r_m}$ should essentially be unity. Localization is implied with Poissonian-like values of $\overline{r_m}$, since localized states can reside in different single-particle basis states of nevertheless similar energies, such that they will not interact or display any significant level repulsion [64]. In the case of the considered two-leg ladder model, we associate the eigenfrequencies ω_m with the energy levels E_m alluded to above, and we apply averaging over equation (27) in order to generate the results presented in figure 3(c). In the map of panel (c), we plot $\overline{r_m}$ as function of both the next-nearest neighbor coupling ratio J_2/J_1 and the inter-chain coupling ratio g/J_1, while the black lines acting as guides for the eye are exactly those of figure 3(a). Notably, the yellow region of figure 3(c) corresponds to an ordered system with $\overline{r_m} \simeq 1$, implying no collections of localized states. Meanwhile, different flavors of extended phases are suggested by the orange and red regions at the top of panel (c), which are approximately encased by the indicative black lines. The lower half of figure 3(c) sees red areas gradually merge into purple islands, in particular the enclosed region ending at $J_2 = J_1$, which are associated with $\overline{r_m} \simeq 0.4$. These kinds of averaged energy level statistics instead suggest a (relatively) more localized phase, as is consistent with the participation ratio map of figure 3(a). Similar conclusions based upon the averaging of the quantity defined in equation (27) have recently been drawn in both theoretical and experimental studies of a variety of other physical systems hosting collections of relatively localized states [66–68].

4. Discussion

In conclusion, we have presented a basic theory for the generation of unconventional edge states in bipartite coupled mode systems due to the presence of asymmetric interactions. We have concentrated on the simplest

case of a two-leg ladder model, where we allowed for different coupling ranges in the upper chain as compared to the lower chain. The long-range coupling leads to additional stationary points developing in the bandstructure which, in a remarkable display of a seemingly non-topological bulk-edge correspondence, predicts the existence of states residing at the edges of the analogous finite-sized lattice. Since these edge states are essentially surrounded by a band of extended states they are in some sense a kind of bound state in the continuum [10–13], albeit generated by the unusual mechanism of asymmetric coupling ranges. Our theoretical predictions could be realized in various physical platforms modeled by lattices with significant next-nearest neighbor interactions, for example with atomic, photonic, phononic and polaritonic setups [27–35]. Perhaps the acoustic metamaterial platform of [28] is the most promising avenue for immediate experimental realization due to its tunability. Finally, although we have concentrated on a toy model of a two-leg ladder for simplicity, our results should generalize to any bipartite systems with asymmetries in their respective couplings, for example matter modes interacting with radiative modes [69–72].

Data availability statement

The code is available at https://github.com/of280/Ladder-Project and is curated by O I R Fox. All data that support the findings of this study are included within the article (and any supplementary files).

Funding

C A D is supported by the Royal Society via a University Research Fellowship (URF R1 201158) and an Exeter-FAPESP SPRINT Grant with the Universidade Federal de São Carlos (state of São Paulo, Brazil). L M M acknowledges the support of Project PID2020-115221GB-C41, which was financed by MCIN/AEI/10.13039/501100011033 and the Aragón Government through Project Q-MAD. OIRF is funded by the EPSRC via the Maths DTP 2021-22 University of Exeter (EP/W523859/1)

Discussions

We thank R Bachelard, A Cidrim, A C Santos, C J Villas-Boas and G Weick for fruitful discussions. We are indebted to Zhen Gao and Ce Shang for constructive discussions surrounding the experimental feasibility of our theoretical proposal, which comes in the wake of their innovative experimental work as described in [28].

Hospitality

C A D is grateful for the support of UFSCar during his visits to São Carlos.

Appendix A. The chain A model

In this appendix we consider the chain A model only, as defined by the Hamiltonian operator $\hat{H}_A$ of equation (2). It describes a linear chain of quantum harmonic oscillators (each of resonance frequency ω_0) interacting with both nearest-neighbor couplings J_1 and—most importantly—also next-nearest-neighbor couplings J_2 (see the sketch of chain A in figure 1(a)). We are especially interested in the continuum limit of a very long chain ($N \to \infty$), and we commonly employ periodic boundary conditions in order to obtain an analytic understanding of both the band theory and the energy level statistics of this subsystem model. In particular, we analyze the additional stationary points in the bandstructure which appear for stronger next-nearest neighbor couplings, we present a detailed derivation of the analytic form of the density of states beyond nearest-neighbor interactions, and we explore in detail the probability density function of adjacent energy levels.

The exponential Fourier transform of equation (5) immediately diagonalizes the chain A Hamiltonian of equation (2), which reveals the eigenfrequencies ω_q^A associated with the quantum number q as follows

$$\hat{H}_A = \sum_q \omega_q^A a_q^\dagger a_q, \tag{A1}$$

$$\omega_q^A = \omega_0 + 2J_1 \cos(qd) + 2J_2 \cos(2qd). \tag{A2}$$

The assumed periodic boundary conditions ensure the 2π-periodicity of the eigensystem, allowing us to focus on the first Brillouin zone $-\pi/d < q \leqslant \pi/d$ only. Essentially, the nonzero inter-site couplings J_1 and J_2 in the chain A model allow for excitations to move throughout the one-dimensional lattice, which gives rise

to kinetic energy terms (cf the second and third terms in equation (A2)) in addition to the onsite energy term of each individual oscillator (cf the first term in equation (A2)). The energy bands formed from ω_q^A are plotted in the first column of figure 4 using equation (A2), for four increasingly large values of the next-nearest neighbor coupling J_2 upon descending the panels (a), (e), (i) and (m). Most notably, with larger next-nearest couplings J_2 in figures 4(i) and (m) the bandstructure exhibits additional stationary points, as marked by colored circles in the figure.

The extrema $\omega_\pm^A$ of the bandstructure defined by equation (A2) are also noticeably affected by sufficiently strong J_2, since the maximum and minimum eigenfrequencies are given by

$$\omega_+^A = \omega_0 + 2\left(J_1 + J_2\right), \tag{A3}$$

$$\omega_-^A = \begin{cases} \omega_{\mathrm{I}}^A, & 0 \leqslant J_2 \leqslant J_1/4, \\ \omega_{\mathrm{II}}^A, & J_1/4 \leqslant J_2 \leqslant J_1. \end{cases} \tag{A4}$$

The maximum eigenfrequency ω_+^A always occurs at the quantum number $q = 0$, irrespective of the value of J_2. However, the minimum eigenfrequency ω_-^A can take on two distinct values, either ω_{I}^A or ω_{II}^A, depending upon the crucial coupling ratio J_2/J_1. Explicitly, we find

$$\omega_{\mathrm{I}}^A = \omega_0 - 2\left(J_1 - J_2\right), \tag{A5}$$

$$\omega_{\mathrm{II}}^A = \omega_0 - 2\left(J_2 + \tfrac{J_1^2}{8J_2}\right). \tag{A6}$$

The state with the quantum number $q = \pi/d$, residing at the edge of the first Brillouin zone, is associated with the band minimum of ω_{I}^A for weaker next-nearest-neighbor couplings satisfying $0 \leqslant J_2 \leqslant J_1/4$, which is demonstrated with the colored dashed lines in figures 4(a) and (e) (cf equation (A5)). For stronger next-nearest-neighbor couplings fulfilling $J_1/4 \leqslant J_2 \leqslant J_1$, the band minimum of ω_{II}^A instead occurs away from the edge of the Brillouin zone at the specific quantum numbers

$$q = \pm\frac{1}{d}\left(\pi - \arctan\left[\sqrt{\left(\tfrac{4J_2}{J_1}\right)^2 - 1}\right]\right), \tag{A7}$$

as marked by the horizontal dashed lines in figures 4(i) and (m) (cf equation (A6)). These bandstructural extrema features of equations (A3) and (A4) (as highlighted by dashed lines throughout the first column of figure 4) as well as the additional stationary points (that is, those stationary points not residing at $qd = 0$ or π, which are represented with colored circles in panels (i) and (m)) together suggest two distinct behavioral regimes for the chain A model, which are separated by the key point in parameter space $J_2 = J_1/4$.

Within standard band theory, the group velocity $v_q^A = \partial_q \omega_q^A$, a measure of how quickly an excitation of energy ω_q^A moves within the lattice, and the inverse effective mass $1/m_q^A = \partial_q^2 \omega_q^A$, a quantifier of how easy it is to accelerate an excitation of energy ω_q^A, follow directly from taking derivatives of the dispersion of equation (A2) with respect to the quantum number q, like so

$$v_q^A = -2d\left[J_1 \sin\left(qd\right) + 2J_2 \sin\left(2qd\right)\right], \tag{A8}$$

$$1/m_q^A = -2d^2\left[J_1 \cos\left(qd\right) + 4J_2 \cos\left(2qd\right)\right]. \tag{A9}$$

These two fundamental quantities are plotted in the second and third columns of figure 4 respectively, and they correspond to the bandstructures ω_q^A plotted in the adjacent panels of the first column of figure 4. In particular, the critical values of q corresponding to additional stationary points in ω_q^A are similarly marked by colored circles in the panels (j) and (n), which are exactly the additional zeroes in the group velocity v_q^A due to the non-negligible next-nearest coupling J_2. Notably, these additional stationary points are also marked by colored circles in the inverse effective mass $1/m_q^A$ plots of panels (k) and (o), which implies that these states have a rather small effective mass m_q^A and hence that they are more prone to moving around the lattice. Importantly, while the inverse effective mass $1/m_q^A$ is a sign-changing quantity as a function of the quantum number q throughout the third column in figure 4, the lowest two panels (k) and (o) have additional roots in the inverse effective mass at certain quantum numbers $q = q^*$, which are relatively near to the Brillouin zone edges (that is, they are not the roots in the vicinity of $qd = \pm\pi/2$). These q^* modes indeed satisfy $1/m_{q^*}^A = 0$, where

$$q^* = \pm\frac{1}{d}\left(\pi - \arctan\left[\frac{\sqrt{128J_2^2 - 2J_1\left(\sqrt{J_1^2 + 128J_2^2} + J_1\right)}}{\sqrt{J_1^2 + 128J_2^2} + J_1}\right]\right). \tag{A10}$$

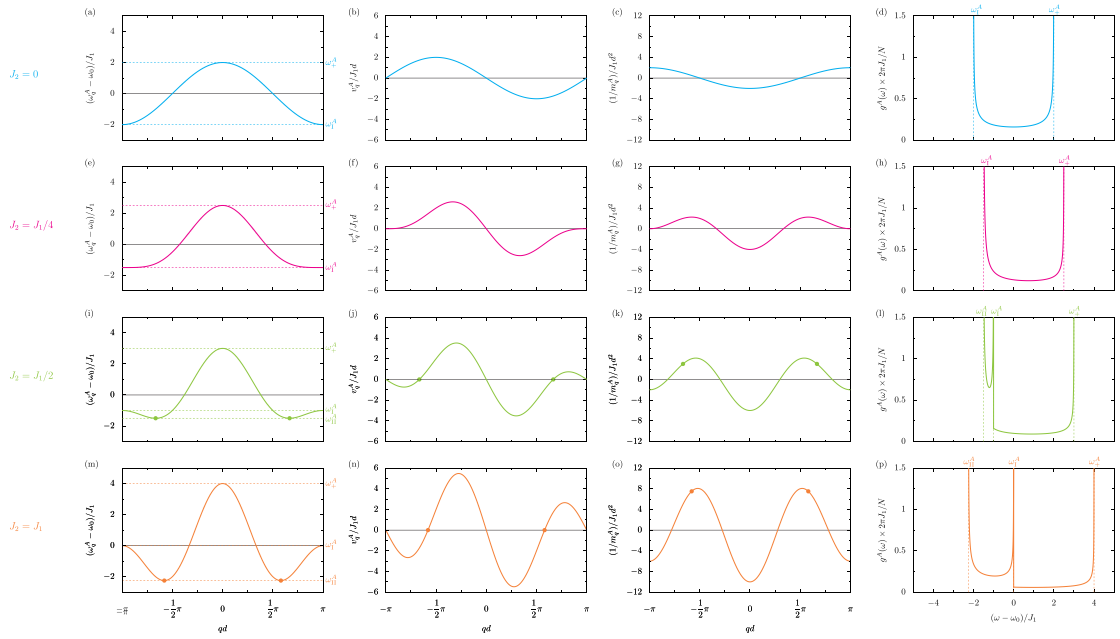

Figure 4. Band properties of the chain A model for an infinite system with periodic boundary conditions. We consider four increasingly large values of the next-nearest neighbor coupling J_2 upon descending the columns of the figure. First column: the bandstructure ω_q^A, as a function of the quantum number q, in the first Brillouin zone $-\pi/d < q \leqslant \pi/d$ (cf equation (A2)). Second column: the associated group velocity v_q^A (cf equation (A8)). Third column: the associated inverse effective mass $1/m_q^A$ (cf equation (A9)). Fourth column: the density of states $g(\omega)$, as a function of frequency ω (cf equation (A23) for $0 \leqslant J_2 \leqslant J_1/4$ and equation (A27) for $J_1/4 \leqslant J_2 \leqslant J_1$). Colored circles in the bottom two rows: critical values of q associated with additional stationary points of ω_q^A (that is, other than those at $q = 0$ and $q = \pi/d$) (cf equation (A7)). Dashed lines in the first and fourth columns: the band maximum ω_+^A (cf equation (A3)) and the eigenfrequencies ω_{I}^A and ω_{II}^A associated with stationary points (cf equations (A5) and (A6)).

These special states with the quantum number q^* correspond to excitations with infinite effective masses, which perhaps implies a greater tendency for them to localize. This is discussed quantitatively later on around equation (A34) and in figure 6(b) when a finite array is considered, and the underpinning mechanism is linked to the ideas of Sajeev John and co-workers [73].

The density of states $g(\omega)$ counts the number of states at a given frequency ω. It is defined for a system of N energy levels, each residing at a certain frequency ω_n, via the informal summation formula

$$g(\omega) = \sum_{n=1}^{N} \delta(\omega - \omega_n), \tag{A11}$$

where $\delta(x)$ is Dirac's delta function, and where the integral over the density of states $\int_{-\infty}^{\infty} g(\omega)\,\mathrm{d}\omega = N$ indeed recovers the total number of energy levels. With regard to the considered Hamiltonian operator $\hat{H}_A$ of equation (A1), where the quantum number $q = 2\pi m/Nd$ due to the employed periodic boundary conditions, one may rewrite equation (A11) in the continuum limit of $N \to \infty$ oscillators as the density of states integral

$$g^A(\omega) = \frac{Nd}{2\pi} \int_{-\frac{\pi}{d}}^{\frac{\pi}{d}} \delta\left(\omega - \omega_q^A\right) \mathrm{d}q, \tag{A12}$$

where the integral is over the whole of the first Brillouin zone, and where the eigenfrequencies ω_q^A are provided by the dispersion relation of equation (A2). The Dirac delta function of some function $f(x)$ is conveniently expressable using the identity

$$\delta[f(x)] = \sum_n \frac{\delta(x - x_n)}{|f'(x_n)|}, \tag{A13}$$

where x_n are the roots of the function $f(x)$ so that $f(x_n) = 0$, and where the first derivative $f'(x) = \frac{\mathrm{d}}{\mathrm{d}x} f(x)$. Working in the dimensionless variable x, and introducing the dimensionless quantity a and the dimensionless coupling strength parameter b, as

$$x = qd, \tag{A14}$$

$$a = \frac{\omega - \omega_0}{2J_1}, \tag{A15}$$

$$b = \frac{J_2}{J_1}, \tag{A16}$$

we may rewrite the argument of the Dirac delta function appearing in the density of states of equation (A12) as follows

$$f(x) = \omega - [\omega_0 + 2J_1 \cos(x) + 2J_2 \cos(2x)]. \tag{A17}$$

Meanwhile the derivative of this function, and its root equation appearing within the delta function identity of equation (A13), can be compactly expressed in the forms

$$f'(x) = 2J_1 [\sin(x) + 2b \sin(2x)], \tag{A18}$$

$$a = \cos(x_n) + b \cos(2x_n). \tag{A19}$$

Upon switching to the new variable $z_n = e^{ix_n}$, the trigonometric equation (A19) is equivalent to the following quartic equation

$$bz_n^4 + z_n^3 - 2az_n^2 + z_n + b = 0. \tag{A20}$$

The four solutions z_n of the quartic equation (A20) are fortunately rather compact, being

$$z_{1,2} = \frac{-1 - \sqrt{1 + 8b(b+a)} \pm \sqrt{2 - 8b(b-a) + 2\sqrt{1 + 8b(b+a)}}}{4b}, \tag{A21}$$

$$z_{3,4} = \frac{-1 + \sqrt{1 + 8b(b+a)} \pm \sqrt{2 - 8b(b-a) - 2\sqrt{1 + 8b(b+a)}}}{4b}. \tag{A22}$$

The solutions of equations (A21) and (A22) imply that there are only two real roots x_n in the case of weak next-nearest coupling $0 \leqslant J_2 \leqslant J_1/4$, so that the integral of equation (A12) can be readily carried out. This procedure leads to the density of states

$$g^A(\omega) = \frac{N}{2\pi J_1} F_+(a,b)\, \Theta\left(\omega - \omega_{\mathrm{I}}^A\right) \Theta\left(\omega_+^A - \omega\right), \tag{A23}$$

which indeed satisfies $\int_{-\infty}^{\infty} g^A(\omega)\, \mathrm{d}\omega = N$. Within equation (A23), $\Theta(x)$ is the Heaviside step function, which takes into account the band extrema at ω_+^A and ω_{I}^A in this weak coupling regime (cf equations (A3) and (A5)), while the two parameters a and b are defined in equations (A15) and (A16) respectively. In writing down the density of states $g^A(\omega)$, we have introduced the auxiliary function $F_+(a,b)$, which is defined through the expression for $F_\pm$ as

$$F_\pm(a,b) = \frac{4b}{\sqrt{2 + 16b(a+b)}\sqrt{4b(b-a) - 1 \pm \sqrt{1 + 8b(a+b)}}}. \tag{A24}$$

Notably, the auxiliary function $F_+(a,b)$ collapses into much simpler forms for the following special values of b, which are the limiting cases

$$F_+(a,0) = \frac{1}{\sqrt{1-a^2}}, \tag{A25}$$

$$F_+\left(a, \tfrac{1}{4}\right) = \frac{2}{\sqrt{3+4a}\sqrt{2\sqrt{6+8a} - 4a - 3}}. \tag{A26}$$

The result of equation (A25) allows for the reproduction of the famous nearest-neighbor coupling only ($J_2 = 0$) result, which features the celebrated van Hove inverse square root singularities at the band edges. The expression of equation (A26) is reached at the largest value of the weak next-nearest coupling regime, $J_2 = J_1/4$. The case of strong next-nearest coupling $J_1/4 \leqslant J_2 \leqslant J_1$ proceeds in a similar fashion to equation (A23), but now all four solutions of equations (A21) and (A22) need to be employed thanks to the additional stationary points. The analogous calculation leads directly to the density of states

$$g^A(\omega) = \frac{N}{2\pi J_1} \left[F_+(a,b)\, \Theta\left(\omega - \omega_{\mathrm{II}}^A\right) \Theta\left(\omega_+^A - \omega\right) + F_-(a,b)\, \Theta\left(\omega - \omega_{\mathrm{II}}^A\right) \Theta\left(\omega_{\mathrm{I}}^A - \omega\right)\right], \tag{A27}$$

where the auxiliary functions $F_{\pm}(a,b)$ are defined in equation (A24). Notably, the effect of the additional stationary points arising due to significant next-nearest coupling J_2 has led to the appearance of a second term in equation (A27) as compared to equation (A23), which creates additional van Hove divergencies in the overall density of states. Using the results of equations (A23) and (A27), we plot the density of states $g^A(\omega)$ in the fourth column of figure 4. The transition from two (panels (d) and (h)) to three (panels (l) and (p)) non-smooth points is readily seen with increasing J_2 as the column descends.

The band theory results discussed here for the chain A model reduce in the limit of nearest-neighbor coupling only ($J_2 \to 0$) to well-known results. In particular, the bandstructure and its extrema, the group velocity, inverse effective mass and the density of states are described by the pleasingly short expressions

$$\omega_q^A = \omega_0 + 2J_1\cos(qd), \tag{A28}$$

$$\omega_+^A = \omega_0 + 2J_1, \tag{A29}$$

$$\omega_-^A = \omega_0 - 2J_1, \tag{A30}$$

$$v_q^A = -2J_1 d\sin(qd), \tag{A31}$$

$$1/m_q^A = -2J_1 d^2\cos(qd), \tag{A32}$$

$$g^A(\omega) = \frac{N}{2\pi J_1}\frac{\Theta\left(\omega-\omega_-^A\right)\Theta\left(\omega_+^A-\omega\right)}{\sqrt{1-\left(\frac{\omega-\omega_0}{2J_1}\right)^2}}, \tag{A33}$$

which all appear graphically in the top row of figure 4 (cyan lines in panels (a)–(d)), where we consider $J_2 = 0$ as the baseline case from which the more complicated behaviors in the lower rows eventually emerge. In particular, the cosine band of equation (A28) leads to standard Van Hove singularities in the density of states of equation (A33) and figure 4(d), which are typical in one-dimensional systems. Clearly from equation (A31), there are only stationary points in the bandstructure at $qd = 0$ and $qd = \pi$, while zeroes of the inverse effective mass only occur at $qd = \pm\pi/2$, as shown graphically in figures 4(b) and (c). In a future study, it may be interesting to consider the influence of the counter-rotating terms [74, 75] discarded from the coupling part of the Hamiltonian, as well as to examine the impact of including an interaction term [76, 77] in the Hamiltonian in order to probe a nonlinear array of anharmonic oscillators.

Thus far, we have exploited periodic boundary conditions and considered the limit of an infinitely large system ($N \to \infty$) in order to study some fundamental band properties of chain A analytically. We shall now consider open boundary conditions with the Hamiltonian operator $\hat{H}_A$ for a finite system of N oscillators, which allows us to study the degrees of localization and energy level statistics of the model. The theoretical treatment requires the diagonalization of the $N \times N$ matrix form of equation (2), which results in a finite number of eigenfrequencies ω_m^A for the countable number of states, which are labeled from $m = \{1, 2, \ldots, N\}$. The values of the associated eigenvectors, on oscillator n and for a state m, are given by the amplitude $c_n^A(m)$. We show some typical eigenfrequency results, as a function of the coupling ratio J_2/J_1, for a chain of $N = 10$ oscillators with the yellow lines in figure 5(a). As a guide for the eye, we include the continuum band edge results of $\omega_{\pm}^A$ as the thick purple lines, using equations (A3) and (A4), which act as the energetic bounds. We see from figure 5(a) how the collection of ten eigenfrequencies ω_m^A evolve with increasing J_2/J_1, and in particular we notice the crucial point around $J_2 = J_1/4$, where the minimum eigenfrequency finally starts to lower due to the appearance of a new stationary point in the analogous infinite system (cf equation (A4)), and where several energy levels start to cluster together, which is important for what follows.

We quantify the degrees of localization of the states m sustained by chain A using the participation ratio $\mathrm{PR}(m)$, as defined in equation (23). Typically, this measure takes the form of $\mathrm{PR}(m) = (2/3)(N+1)$ or similar in conventional, one-dimensional tight-binding systems (as is shown later on in equation (B6)). The linear dependence on N is characteristic of all extended states, while the prevalent prefactor of $2/3$ arises from the geometry of the linear chain with open boundary conditions. In figure 6(a) we are interested in the three measures, all of which are linked to the participation ratio and are scaled by the convenient factor $N+1$, as a function of the coupling ratio J_2/J_1. The red line in figure 6(a) denotes $\max\{\mathrm{PR}(m)\}$, the maximum of the participation ratios (found after consideration of all states m). With vanishing J_2 and for $J_2 > J_1/2$, this quantity is essentially the constant $\max\{\mathrm{PR}(m)\}/(N+1) \simeq 2/3$ (this relation is exact for $J_2 = 0$). This implies a linear relationship between the participation ratio and the system size, while the $2/3$ prefactor is typical of extended states. Interestingly, for $0 < J_2 < J_1/2$ a larger prefactor associated with $\max\{\mathrm{PR}(m)\}$ is demonstrated, which perhaps indicates the presence of some unusually super-extended states due to the non-negligible next-nearest neighbor hoppings. Similarly, the yellow line in figure 6(a) denotes $\min\{\mathrm{PR}(m)\}$, graphing the minimum of the participation ratio (over all states m) scaled by $N+1$. The additional stationary points suddenly occurring around $J_2 = J_1/4$ are seemingly correlated with an

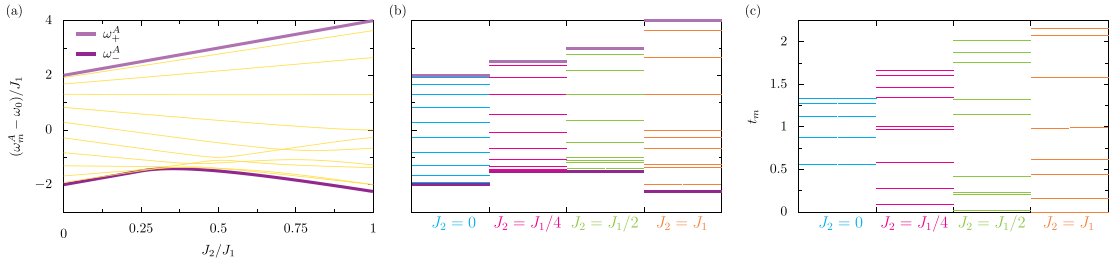

Figure 5. Eigenfrequencies of the chain A model for a finite system with open boundary conditions. Panel (a): the eigenfrequencies ω_m^A for a finite system of $N = 10$ oscillators, as a function of the next-nearest neighbor coupling J_2 (in units of the nearest neighbor coupling J_1), as marked by the yellow lines. Thick purples lines: $\omega_\pm^A$, the extrema of the equivalent band formed in the continuum limit $N \to \infty$ (cf equations (A3) and (A4)). Panel (b): the specific eigenfrequencies ω_m^A, taken from panel (a) at the chosen values of $J_2/J_1 = \{0, 1/4, 1/2, 1\}$, as associated with the cyan, pink, green and orange lines respectively. Purple lines: the extrema $\omega_\pm^A$ in the continuum limit. Panel (c): the relative energy level spacings t_m between the eigenfrequencies ω_m^A taken from panel (b).

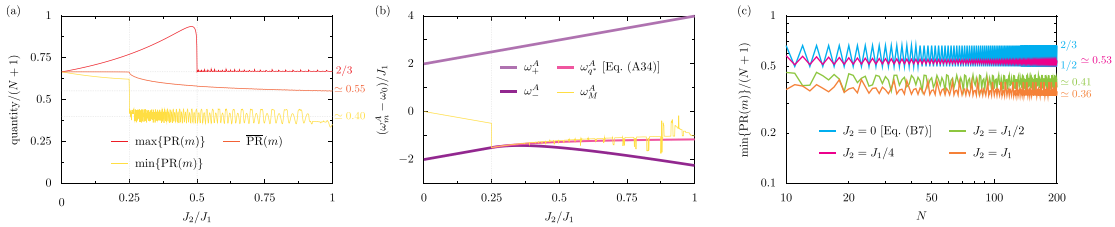

Figure 6. Degrees of localization in the chain A model. Panel (a): various localization measures, scaled by $N + 1$, related to the participation ratio $\mathrm{PR}(m)$ of a state m. We plot as a function of the next-nearest neighbor coupling J_2 (in units of the nearest neighbor coupling J_1), and here we consider a finite system of $N = 300$ oscillators. Red line: $\max\{\mathrm{PR}(m)\}$, the maximum of the participation ratios of all states m. Orange line: $\overline{\mathrm{PR}(m)}$, the mean value of the participation ratios. Yellow line: $\min\{\mathrm{PR}(m)\}$, the minimum of the participation ratios. Panel (b): some chosen eigenfrequencies as a function of J_2. Thin yellow line: the specific eigenfrequency ω_M^A corresponding to the state with the index M, that with the smallest participation ratio. Pink line: the eigenfrequency $\omega_{q^*}^A$, corresponding to the state with the quantum number q^*, which is associated with the appearance of an additional root in the inverse effective mass in the continuum limit (cf equation (A34)). Purple lines: $\omega_\pm^A$, the extrema of the continuum model band (cf equations (A3) and (A4)). Panel (c): a log-log plot of the minimum of the scaled participation ratio $\min\{\mathrm{PR}(m)\}/(N+1)$ as a function of the system size N. We consider the coupling ratios $J_2/J_1 = \{0, 1/4, 1/2, 1\}$ with the cyan, pink, green and orange lines respectively. The result for $J_2 = 0$ (cyan line) is analytic (cf equation (B7)).

unusually low prefactor of ~ 0.4 in this case, which may perhaps be termed sub-extended states since the linear scaling with N is maintained, but less than one half of the total number of sites are felt by the state. Finally, the mean of the participation ratio $\overline{\mathrm{PR}(m)}$, calculated as the average over all N states, is represented by the orange line in figure 6(a). The orange curve suggests that the average state does not behave all that differently below and above the critical coupling of $J_2/J_1 = 1/4$.

The calculations leading to the results of figure 6(a) were carried out for a finite chain of $N = 300$ oscillators, which also led to the results of panel figure 6(b). There we plot some key eigenfrequencies as a function of the coupling ratio J_2/J_1. Similarly to figure 5(a), the purple lines mark the continuum band edges $\omega_\pm^A$ as a guide for the eye at the energetic bounds. More importantly, the yellow line in figure 6(b) tracks the special eigenfrequency ω_M^A, coming from the particular state $m = M$ with the smallest participation ratio $\min\{\mathrm{PR}(m)\}$. For the important coupling regime of $J_1/4 < J_2 < J_1$, where the participation ratio of the state M is appreciably smaller than for all other states (cf figure 6(a)), the key eigenfrequency ω_M^A is remarkably seen to be not too dissimilar to the analytic expression

$$\omega_{q^*}^A = \omega_0 - \frac{3J_1}{32J_2}\left(J_1 + \sqrt{J_1^2 + 128J_2^2}\right), \tag{A34}$$

as plotted with the pink line in figure 6(b). We arrived at equation (A34) by substituting the specific the quantum number $q = q^*$ (cf equation (A10)), which is associated with a zero in the inverse effective mass $1/m_q^A$ from equation (A9), into the bandstructure of equation (A2). The approximate likeness of ω_M^A and equation (A34), as suggested by figure 6(b), can be interpreted as this particular excitation with q^* having a large effective inertia, such that the state is much more resistant to extending over the entire one-dimensional array of coupled oscillators.

We confirm the extended nature of all of the states sustained in the chain A model in figure 6(c), which plots the minimum of the scaled participation ratio $\min\{\mathrm{PR}(m)\}/(N+1)$ as a function of the overall system size N. We consider four values of J_2, corresponding to the four cases considered previously in figure 4. Clearly, all of the cases quickly tend towards constant values, revealing the linear dependence of this localization measure with the total number of oscillators N in the chain. In particular, the case of $J_2 = 0$ (cyan line) is describable analytically (as shown later on in equation (B7), prompting the choice of scaling with $N+1$ rather than simply N) and it exhibits a triangular waveform due to an even–odd relationship with the system size N.

The energy level statistics of chain A are investigated in figure 7. In particular, we consider two closely related quantities describing energy level correlations in figures 7(a) and (b) [62, 63]. Meanwhile figure 7(c) is focussed on the statistics of consecutive energy level spacings [64, 65], as was also investigated in figure 3(c) for the two-leg ladder model of the main text. We previously described with yellow lines in figure 5(a) the eigenfrequencies ω_m^A, as a function of the coupling ratio J_2/J_1, for a relatively small chain of $N = 10$ oscillators. Taking four cuts through figure 5(a) at the coupling ratios $J_2/J_1 = \{0, 1/4, 1/2, 1\}$ results in the energy level diagram sketched in figure 5(b), where some level clusterings become more obviously apparent than in figure 5(a). With these energy levels $E_m = \omega_m^A$, ordered such that $m = 1$ corresponds to the smallest eigenfrequency and ascending to the largest eigenfrequencies when $m = N$, we may define the $N-1$ energy level separations $S_m = E_{m+1} - E_m$, where the index $m = \{1, 2, \ldots, N-1\}$. The mean energy level spacing is the average of these energetic distances $D = \overline{S_m}$, such that one may define the $N-1$ normalized energy level spacings $t_m = S_m/D$. We plot these normalized and dimensionless energy level spacings t_m in figure 5(c), corresponding to the eigenfrequencies of figure 5(b). In the thermodynamic limit of $N \to \infty$, the distribution of t_m can then be described within the statistical theory of energy levels [62, 63] as we now discuss.

The cumulative distribution function $C(t)$ of the adjacent energy levels, as a function of the continuum energy level spacing t, is plotted in figure 7(a) for four representative values of J_2 within the chain A model. There are no energy level spacings with a spacing below a vanishing amount such that $C(t \to 0) = 0$, while for some sufficiently large value of the dimensionless energy level spacing $t = T$ all energy level spacings in the chain A model should be smaller than it (due to the collection of energy levels packing themselves into an effective band), such that $C(t \geqslant T) = 1$. The simplest case of $J_2 = 0$ is denoted by the cyan line in figure 7(a), whose cumulative distribution curve is obtained analytically with the exact inverse trigonometric expression

$$C(t) = \frac{2}{\pi} \arcsin\left(\frac{2t}{\pi}\right) \Theta\left(\tfrac{\pi}{2} - t\right) + \Theta\left(t - \tfrac{\pi}{2}\right), \tag{A35}$$

where the threshold dimensionless energy level spacing $T = \pi/2$, as is marked at the top of figure 7(a). The derivation of equation (A35) is provided later on in appendix B, where the chain B model is analyzed. The results for three other cases with $J_2 \neq 0$, corresponding to the values considered in figures 5(b) and (c), are shown in figure 7(a) after a numerical calculation for a finite system composed of $\mathrm{N} = 15\,000$ oscillators. This leads to successively larger values energy level spacings T for which $C(T) = 1$ first occurs, due to the increasingly large bandwidths of the effective bands formed by the collections of energy levels. These approximate threshold T values are noted at the top of figure 7(a).

The probability density functions $p(s)$ associated with the four curves of figure 7(a), such that the integral $\int_0^t p(s)\,\mathrm{d}s = C(t)$, are plotted in figure 7(b). The probability density function $p(s)$ in the simplest case of $J_2 = 0$ follows from taking the derivative of equation (A35) with respect to t and evaluating the result at the dimensionless value s, leading to the neat formula

$$p(s) = \frac{2}{\pi} \frac{\Theta\left(\frac{\pi}{2} - s\right)}{\sqrt{\left(\frac{\pi}{2}\right)^2 - s^2}}, \tag{A36}$$

which indeed satisfies the normalization $\int_0^\infty p(s)\,\mathrm{d}s = 1$ in order to conserve the total probability. Furthermore, the first moment obeys $\int_0^\infty sp(s)\,\mathrm{d}s = 1$, since the mean level spacing was normalized to unity. The inverse-square root distribution of equation (A36) is shown by the cyan line figure 7(b), demonstrating a lack of energy level repulsion since $p(s \to 0) = (2/\pi)^2 \simeq 0.405$. This is followed by an increasing likelihood of larger level separations until the critical value of $s = \pi/2$ is reached, after which there is a step function drop-off to zero due to the finite bandwidth of the chain A model. The rough numerical results for the three nonzero values of J_2 considered in figure 7(a) are also shown in figure 7(b), which display significantly enhanced clusterings of the energy levels due to the $s \to 0$ behavior, as was already hinted at in the level spacing diagram of figure 5(c). The critical behavior (abrupt dropping to zero) of the $J_2 \neq 0$ cases in figure 7(b) appears at increasingly large values of s, as is expected from the analytic case of $J_2 = 0$ and equation (A36), where the criticality lies at $s = \pi/2$.

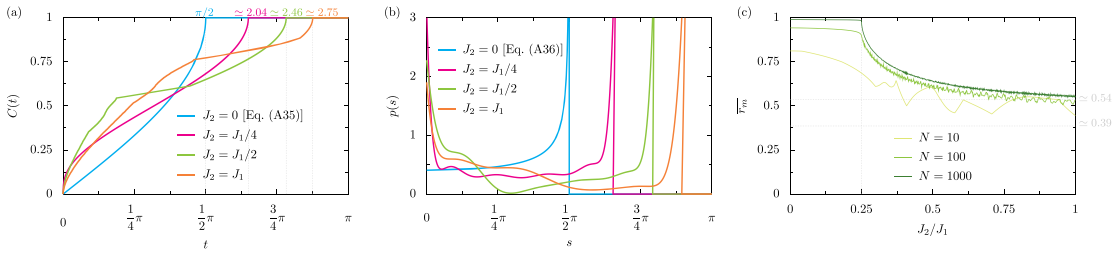

Figure 7. Energy level statistics of the chain A model. Panel (a): the cumulative distribution function $C(t)$ for the adjacent energy level spacings, for the four coupling ratios J_2/J_1 also considered in figure 6(c). Panel (b): the probability density function $p(s)$ associated with the results of panel (a), so that $\int_0^t p(s)\,\mathrm{d}s = C(t)$. We consider a finite system of $N = 15\,000$ oscillators in panels (a) and (b) for the cases with $J_2 \neq 0$, otherwise we use the analytic expressions of equation (A35) and (A36) for the case of $J_2 = 0$ (cyan lines in both panels). Panel (c): the mean value of the ratio of consecutive energy level spacings $\overline{r_m}$, as a function of J_2. We consider three increasingly large finite systems with $N = \{10, 100, 1000\}$ oscillators. Dashed grey lines: the values $2\ln 2 - 1 \simeq 0.39$ (associated with Poissonian level statistics and a localized phase) and $4 - 2\sqrt{3} \simeq 0.54$ (associated with Gaussian orthogonal ensembles and an extended phase).

For a given spectrum, the ratio of consecutive energy level spacings r_m, as defined by equation (27), provides a measure of the correlations between adjacent energy level gaps [64]. The mean value $\overline{r_m}$ provides a certain sense of the degree of chaoticity, being essentially unity in ordered models and dropping to $\overline{r_m} = 2\ln 2 - 1 \simeq 0.39$ for models with Poissonian level statistics, which sometimes implies a more localized phase [57, 65]. The evolution of mean ratio $\overline{r_m}$ for the chain A model with the coupling ratio J_2/J_1 is depicted in figure 7(c). We consider the results for three increasingly large magnitudes of the finite system size N with increasingly dark green lines. Strikingly, while for weak next-nearest couplings $J_2 < J_1/4$ the thermodynamic limit of $N \to \infty$ sees the mean ratio approach $\overline{r_m} = 1$, corresponding to an ordered system, the regime of strong next-nearest couplings $J_1/4 < J_2 \leqslant J_1$ is characterized by a decay from unity. This drop-off starts abruptly at the key coupling $J_2 = J_1/4$, falling towards a value of $\overline{r_m} \simeq 0.55$ when $J_2 = J_1$ (in the thermodynamic $N \to \infty$ limit). This mean value $\overline{r_m}$ is somewhat similar to the case of a Gaussian orthogonal ensemble, where $\overline{r_m} = 4 - 2\sqrt{3} \simeq 0.54$ [78], suggesting a kind of extended phase in the chain A model which is consistent with the participation ratio results of figure 6.

Appendix B. The chain B model

In this appendix we consider the chain B model as defined by the Hamiltonian operator $\hat{H}_B$ of equation (3), describing a finite linear chain of N quantum harmonic oscillators (each of resonance frequency ω_0) interacting via nearest-neighbor coupling (of strength J_1) only (see the sketch of chain B in figure 1(a)). In particular, we are interested in analytical descriptions of the various degrees of localization arising in this simple system, as judged by the participation ratio [57, 58], and the energy level statistics resulting from the chain B Hamiltonian, as governed by the probability density function for its adjacent energy level spacings [79–81]. The mathematical results provided here provide an understanding of the more general chain A model (cf appendix A) in the limit of vanishing J_2, and also impart some intuition about the behavior of the more complicated chain A-B model considered throughout the main text.

Diagonalization of the finite system described by equation (3), with the implied open boundary conditions, is best carried out by employing the following discrete sine transform (and its inverse) for the bosonic annihilation and creation operators b_n and $b_n^\dagger$, where

$$b_n = \sqrt{\tfrac{2}{N+1}} \sum_{k_m} \sin\left(n k_m d\right) b_{k_m}, \tag{B1}$$

$$b_{k_m} = \sqrt{\tfrac{2}{N+1}} \sum_{n=1}^{N} \sin\left(n k_m d\right) b_n, \tag{B2}$$

where we have introduced the quantum number k_m, where the dimensionless quantity $k_m d = \pi m/(N+1)$ and the integer $m \in [1, N]$. Substitution of equation (B1) into equation (3) yields the diagonalized Hamiltonian operator $\hat{H}_B$, and its associated eigenfrequencies $\omega_{k_m}^B$, as follows

$$\hat{H}_B = \sum_{k_m} \omega_{k_m}^B b_{k_m}^\dagger b_{k_m}, \tag{B3}$$

$$\omega_{k_m}^B = \omega_0 + 2J_1 \cos\left(k_m d\right). \tag{B4}$$

Clearly, in the thermodynamic limit of $N \to \infty$ the eigenfrequencies of equation (B4) form a continuous band of allowed energies (cf equation (A2) with $J_2 = 0$). The probability amplitudes $c_n^B(m)$ of each state m, for every site n in the chain, follow from the diagonalizing operator b_{k_m} of equation (B2) as $c_n^B(m) = \langle 1_n | b_{k_m}^\dagger | \text{vac} \rangle$, where $|\text{vac}\rangle = |0, \ldots, 0\rangle$ is the vacuum state. We use the notation that $|1_n\rangle$ corresponds to a single excitation on site n only, so that $|1_1\rangle = |1, \ldots, 0\rangle$ and $|1_N\rangle = |0, \ldots, 1\rangle$ for example. Then the explicit form of the probability amplitudes $c_n^B(m)$ is

$$c_n^B(m) = \sqrt{\tfrac{2}{N+1}} \sin(n k_m d). \tag{B5}$$

Substitution of equation (B5) into the formula of equation (23) yields the exact participation ratio $\text{PR}(m)$ for a state m as follows

$$\text{PR}(m) = \begin{cases} \frac{2}{3}(N+1), & m \neq \frac{N+1}{2}, \\ \frac{1}{2}(N+1), & m = \frac{N+1}{2}, \end{cases} . \tag{B6}$$

As expected, all of the states m are extended due to the explicit linear relationship between the participation ratio and the system size N. Essentially, the relationship $\text{PR}(m) \simeq (2/3)N$ holds for almost all states (the sole exception is for the single state with the eigenfrequency exactly at ω_0, which only occurs for a chain with an odd number N of oscillators). This general prefactor of $2/3$ is typical of extended states and its fingerprints also appear in the chain A-B model via the dark green line in figure 2(c) and in the blue region in figure 3(a), as well as for the chain A model via the red line (for $J_2 \geqslant J_1/2$) in figure 6(a). Upon dividing the result of equation (B6) by the convenient number $N+1$, it follows that the minimum (taken over all states m) possible scaled participation ratio for this chain B system is simply

$$\frac{\min\{\text{PR}(m)\}}{N+1} = \begin{cases} 1/2, & N \text{ odd}, \\ 2/3, & N \text{ even}, \end{cases} . \tag{B7}$$

The formula of equation (B7) defines a triangular waveform relationship of the least extended state with increasing system size N, as was already demonstrated graphically by the cyan line in figure 6(c).

Let us now consider some statistical properties of the energy levels [62, 63] of the chain B model, using the exact eigenfrequencies $\omega_{k_m}^B$ from equation (B4). We start by reordering these N energy levels, now relabeled as E_m for simplicity, in the ascending order $E_1 < E_2 < E_3 \ldots$ like so

$$E_m = \omega_0 + 2J_1 \cos\left(\pi \frac{N+1-m}{N+1}\right), \tag{B8}$$

where the index $m = \{1, 2, \ldots, N\}$. There are then $N-1$ adjacent energy level separations $S_m = E_{m+1} - E_m$, which read

$$S_m = 2J_1 \left\{ \cos\left(\pi \frac{N-m}{N+1}\right) - \cos\left(\pi \frac{N+1-m}{N+1}\right) \right\}, \tag{B9}$$

whose index spans $m = \{1, 2, \ldots, N-1\}$. The mean value of these adjacent energy level separations $D = \overline{S_m}$ is given by

$$D = \frac{2J_1}{N-1} \left\{ \cos\left(\frac{\pi}{N+1}\right) - \cos\left(\frac{N\pi}{N+1}\right) \right\}, \tag{B10}$$

such that the normalized energy level spacings $t_m = S_m/D$ are completely defined via the formula

$$t_m = (N-1) \frac{\cos\left(\pi \frac{N-m}{N+1}\right) - \cos\left(\pi \frac{N+1-m}{N+1}\right)}{\cos\left(\frac{\pi}{N+1}\right) - \cos\left(\frac{N\pi}{N+1}\right)}. \tag{B11}$$

There are $N-1$ values of the normalized energy level spacings t_m. For an odd number N of oscillators in the chain, the values of t_m for the reduced set $m = \{1, 2, \ldots, (N-1)/2\}$ perfectly match with the values of t_m obtained from the remaining set where $m = \{N, N-1, \ldots, (N+1)/2\}$. Therefore, since we are ultimately only interested in the thermodynamic limit of $N \to \infty$, we assume N is odd and restrict the index of t_m to $m = \{1, 2, \ldots, (N-1)/2\}$ only in what follows. Since each normalized energy level spacing t_m within this restricted index range of m is both unique and runs in ascending order, the number of energy level spacings within some range S increases from zero one-by-one after passing the increasing values of t_1, t_2, t_3 and so on

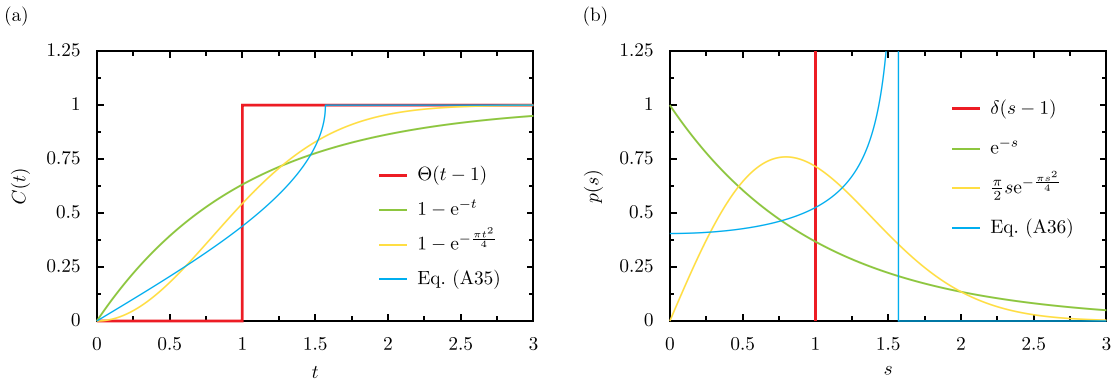

Figure 8. A comparison of the energy level statistics of the chain B model with some celebrated models. Panel (a): the cumulative distribution function $C(t)$ as a function of the dimensionless energy level spacing t for four different models. Panel (b): the probability density functions $p(s)$ corresponding to the curves of panel (a). Red lines: the picket fence model, where the equal energy level spacing leads to a Dirac delta function distribution. Green lines: the uncorrelated energy levels model, where the random energy level spacing leads to a Poisson distribution. Yellow lines: a chaotic model, where the Gaussian orthogonal ensemble leads to the simplest type of Wigner distribution. Cyan lines: the chain B model, as described analytically by the cumulative and density functions of equations (A35) and (A36) respectively.

with increasing S, up to the largest energy level spacing $t_{(N-1)/2}$. Hence the fraction of all energy level spacings (there are a total of $(N-1)/2$ energy level spacings in this analysis) with an energy level spacing below a certain t_m is $C_m = 2(m-1)/(N-1)$. That is, there are zero energy level spacings with a spacing smaller than t_1 and so the fraction $C_1 = 0$, while there are $(N-3)/2$ energy level spacings with a spacing smaller than $t_{(N-1)/2}$ and so the fraction $C_{(N-1)/2} = 1 - 2/(N-1)$. Let us now take the thermodynamic limit of $N \to \infty$ with the normalized energy level spacings t_m of equation (B11), which yields the simplification

$$t_m = \frac{\pi}{2} \sin\left(\frac{m\pi}{N+1}\right), \tag{B12}$$

which, due to the restricted index $m = \{1, 2, \ldots, (N-1)/2\}$, has the bounds $0 \leqslant t_m \leqslant \pi/2$. Within this thermodynamic limit, the fractional counting quantity $C_m = 2(m-1)/(N-1)$ similarly satisfies the expected continuous range $0 \leqslant C_m \leqslant 1$. Then, upon explicitly eliminating the index m in equation (B12) with the help of C_m, and noting that we are working within the continuum limit of $N \to \infty$, we finally arrive at the desired continuum result

$$t = \frac{\pi}{2} \sin\left(\frac{\pi}{2} C\right), \tag{B13}$$

where we have replaced t_m and C_m with their continuous counterparts: the normalized energy level spacing t and the cumulative probability C, which naturally fulfills the proper range $0 \leqslant C \leqslant 1$. The inversion of equation (B13) provides the equation for the probability $C(t)$ directly, as was already quoted in equation (A35). We also sketch equation (A35) with the cyan line in figure 8(a), alongside the cumulative distribution functions of some other celebrated models. The picket fence model with equal energy level spacings necessitates a step function behavior (red line), the uncorrelated energy levels model with random energy level spacings yields a smooth step function (green line), and a chaotic model described by a Gaussian orthogonal ensemble essentially exhibits a Gaussian function (yellow line) [62, 63].

The probability density function $p(s)$ associated with equation (B13) was given in equation (A36), and it is represented by the cyan line in figure 8(b) along with the other distributions corresponding to the cumulative curves of figure 8(a). Namely, the picket fence model has a Dirac delta function distribution (red line) due to the completely equal level spacings, while the uncorrelated model has a Poisson distribution (green line) implying that small level spacings are highly likely since $p(s \to 0) = 1$, while large level spacings are vanishingly unlikely with an exponential fall-off $p(s) = \mathrm{e}^{-s}$. The chaotic model has a Wigner distribution (yellow line) which suggests significant energy level repulsion due to the behavior $p(s \to 0) = 0$, along with vanishing chances for large level spacings due to the very fast Gaussian decay $p(s \to \infty) \simeq \mathrm{e}^{-\pi s^2/4}$. Interestingly, the inverse-square root distribution of the chain B model as described by equation (A36) (cyan line) demonstrates the absence of energy level repulsion since $p(s \to 0) = (2/\pi)^2 \simeq 0.405$, after which increasingly large level separations are increasingly likely up to the critical value of $s = \pi/2$. Above this value there is a brutal step function drop-off to zero due to the effective formation of a finite cosine band of energy levels (cf equation (B4)).

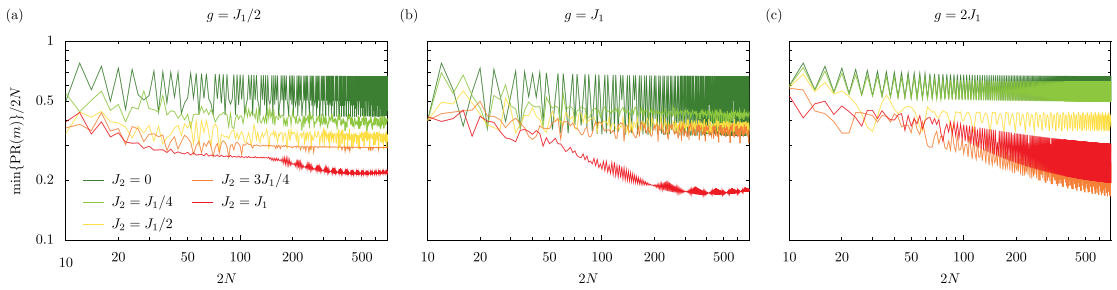

Figure 9. Finite size effects in the two-leg ladder model. Log-log plots of the minimum (taken over all eigenstates m) of the scaled participation ratio $\mathrm{PR}(m)/2N$ as a function of $2N$, the total number of oscillators in the chain A–B system (cf equation (23)). We consider three values of the inter-chain coupling strength g across the three panels of the figure, and five values of the next-nearest neighbor coupling strength J_2 in each case (as marked by the plot legend in the first panel). Panel (a): $g = J_1/2$. Panel (b): $g = J_1$. Panel (c): $g = 2J_1$. This figure supplements the results of figure 3(b) in effectively taking horizontal cuts through figure 3(a) at three values of g, followed by vertical cuts at five values of J_2, and then extending the outcome as a function of the system size $2N$ (up to $2N = 700$).

Appendix C. The chain A–B model

In this appendix we house some additional calculations for a finite-sized two-leg ladder which, in the same manner as figure 3(b), aids the interpretation of the overall participation ratio map for the chain A–B model as given in figure 3(a). In essence, we take three horizontal cuts through the map of figure 3(a) at certain values of the inter-chain coupling strength g, followed by vertical cuts at five values of the next-nearest neighbor coupling strength J_2, before we then extend the results as a function of the system size $2N$, the total number of oscillators in the system, to finally realize the desired plots. The outcomes are displayed in the three log–log plots of figure 9, where we plot the minimum (taken over all eigenstates m) of the scaled participation ratio $\min\{\mathrm{PR}(m)\}/2N$ as a function of $2N$ (cf equation (23)).

We consider three increasingly large values of g across the three panels of figure 9, and we pick out five values of J_2 in each case (as marked by the plot legend in the first panel). Characteristically, across all of the panels in figure 9 we notice that when J_2 is sufficiently small (darker green, lighter green and yellow lines) all eigenstates m have participation ratios $\mathrm{PR}(m)$ which scale essentially linearly with the system size $2N$, with only the prefactor changing from ~ 0.7 to ~ 0.3. In figures 9(a) and (b), where the inter-chain coupling strength $g = J_1/2$ and $g = J_1$ respectively, the cases of maximal next-nearest coupling $J_2 = J_1$ (red lines) display seemingly weakly sublinear scalings in this range of system size up to $2N = 700$, which is consistent with the interpretation of the participation ratio map of figure 3(a). The protruding feature on the right-hand-side of figure 3(a) is supported by the results of figure 9(c), where now $g = 2J_1$, which shows that the two largest values of J_2 (orange and red lines) are both associated with edge states rather than extended states, as implied by the apparent sublinear scalings of the participation ratio $\mathrm{PR}(m)$ with the system size $2N$ (for the values of $2N$ considered). We do not enter a discussion of even larger system sizes, since these cases fall outside of the current experimental scope of coupled systems with tunable next-nearest neighbor coupling [27–29]. Finally, the highly non-monotonic data presented in figure 9 is strongly influenced by the exact value of the integer $2N$ describing the system size. We do not provide a commentary on the number theory of the presented model here, except to note the clear even–odd effect in the simplified chain B model (as discussed around equation (B7)).

Appendix D. The chain A–B model with detuning

In this appendix we consider a small generalization of the model of the main text in order to allow for a difference in resonance frequency between the oscillators of chain A and chain B. Instead of the common resonance frequency ω_0 for all oscillators in the two-leg ladder (cf equations (2) and (3)), we suppose that the resonators in the upper chain are associated with the frequency ω_A, while those in the lower chain are instead describable with the frequency ω_B. The inter-chain detuning D, where

$$D = \omega_A - \omega_B, \tag{D1}$$

of the bipartite system then becomes a meaningful parameter. We provide some information about the degrees of localization in this slightly generalized model in figure 10, which presents participation ratio maps in the style of figure 3(a) from the main text but now for different values of the detuning parameter D (for the case of a two-leg ladder with $2N = 200$ oscillators). The central panel (c) in figure 10 (where $D = 0$)

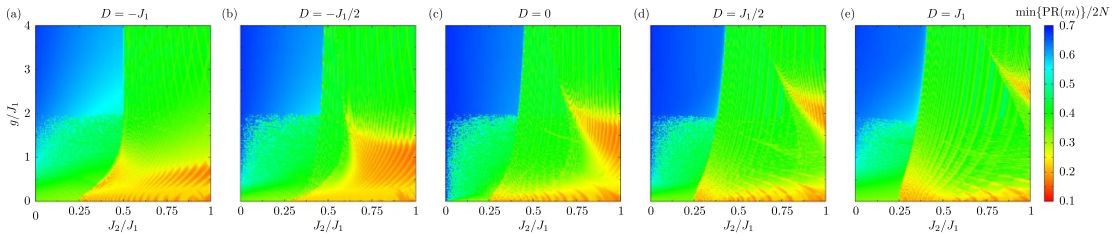

Figure 10. Degrees of localization in the two-leg ladder model with detuning. Maps of the minimum of the scaled participation ratio $\min\{\mathrm{PR}(m)\}/2N$, as a function of both the inter-chain coupling strength g and the next-nearest neighbor coupling strength J_2, both in units of the nearest-neighbor coupling J_1 (cf equation (23)). We consider five different detunings $D = \omega_A - \omega_B$, defined via the resonance frequencies ω_A and ω_B of the oscillators in the upper chain and lower chain respectively, across the row of panels as marked as the top of the figure. The case of the central panel (c) recovers the model of the main text, where $D = 0$ (since $\omega_A = \omega_B = \omega_0$). In this figure, we consider a two-leg ladder with $2N = 200$ oscillators.

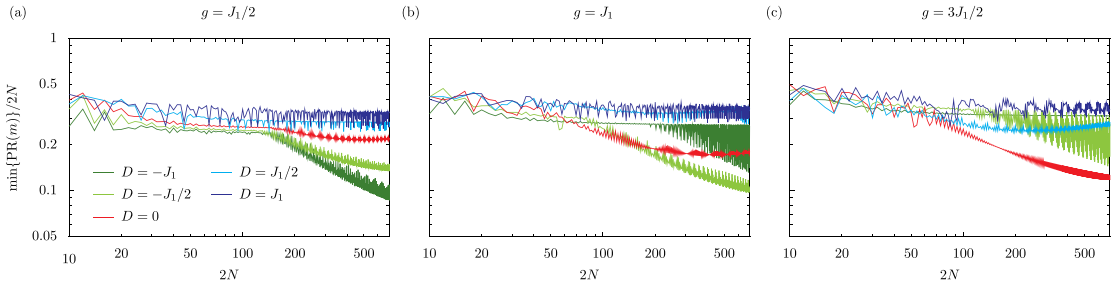

Figure 11. Finite size effects in the two-leg ladder model with detuning. Log-log plots of the minimum (taken over all eigenstates m) of the scaled participation ratio $\mathrm{PR}(m)/2N$ as a function of $2N$, the total number of oscillators in the chain A–B system with detuning (cf equation (23)). We consider five values of the inter-chain detuning D (as marked by the plot legend in panel (a)), corresponding to the values in figures 10(a)–(e). This figure supplements the results of figure 10 by effectively taking horizontal cuts through figures 10(a)–(e) at three values of g (as marked at the top of this figure) and a single vertical cut at $J_2 = J_1$, and then extending the outcome as a function of the system size $2N$ (up to $2N = 700$).

repeats the zero detuning results of figure 3 (a), while panels (a) and (b) show the impact of negative detunings ($D < 0$). Panels (d) and (e) in figure 10 similarly show the consequences of positive detunings ($D > 0$). Most noticeably, the principle features seen in figure 10(c) are also observable in panels (a), (b), (d) and (e), but clearly it is preferable to have a negative detuning as in figures 10(a) and (b) in order to create a larger red-orange zone where edge states reside.

We track the finite-size effects associated with figure 10 in figure 11, which takes cuts at $J_2 = J_1$ and at three values of the inter-chain coupling g across figures 11(a)–(c), for the five cases of detuning D already considered in figure 10. The special case of zero detuning ($D = 0$) is shown in red, two negative detunings ($D < 0$) are represented with green lines and two positive detunings ($D > 0$) are displayed with blue lines. In figure 11(a), where $g = J_1/2$, the cases with negative detuning (light and dark green lines) clearly display a sublinear scaling with the system size in this range up to $2N = 700$, as was already anticipatable from figure 10. When $g = J_1$ in figure 11(b), the $D = -J_1/2$ case (light green line) is particularly sublinear, suggesting that some amount of detuning can be beneficial for the creation of edge states with a stronger degree of localization. Finally in figure 11(c), where $g = 3J_1/2$, the zero detuning case (red line) shows gently oscillating sublinear behavior, as opposed to the strong oscillations observable when $D = -J_1/2$ (light green line), which points to the non-trivial size-dependencies arising in the two-leg ladder model even for $2N \sim 10^3$. Importantly, the results presented in this appendix suggest that the particular flavor of edge state introduced in the main text is indeed robust against nonzero onsite energy detunings, improving the perspectives for future experimental detection.

ORCID iDs

C A Downing https://orcid.org/0000-0002-0058-9746
L Martín-Moreno https://orcid.org/0000-0001-9273-8165

References

[1] Anderson P W 1958 Absence of diffusion in certain random lattices *Phys. Rev.* **109** 1492
[2] Thouless D J 1974 Electrons in disordered systems and the theory of localization *Phys. Rep.* **13** 93–142
[3] Wiersma D S 2013 Disordered photonics *Nat. Photon.* **7** 188
[4] Segev M, Silberberg Y and Christodoulides D N 2013 Anderson localization of light *Nat. Photon.* **7** 197
[5] Wannier G H 1962 Dynamics of band electrons in electric and magnetic fields *Rev. Mod. Phys.* **34** 645
[6] Emin D and Hart C F 1987 Existence of Wannier-Stark localization *Phys. Rev.* B **36** 7353
[7] Arikawa M, Tanaya S, Maruyama I and Hatsugai Y 2009 Edge states of a spin-1/2 two-leg ladder with four-spin ring exchange *Phys. Rev.* B **79** 205107
[8] Hasan M Z and Kane C L 2010 Colloquium: topological insulators *Rev. Mod. Phys.* **82** 3045
[9] Asboth J K, Oroszlany L and Palyi A 2016 *A Short Course on Topological Insulators* (Springer) (arXiv:1509.02295)
[10] Hsu C W, Zhen B, Stone A D, Joannopoulos J D and Soljačić M 2016 Bound states in the continuum *Nat. Rev. Mater.* **1** 16048
[11] Azzam S I and Kildishev A V 2020 Photonic bound states in the continuum: from basics to applications *Rep. Prog. Phys.* **9** 2001469
[12] Sadreev A F 2021 Interference traps waves in an open system: bound states in the continuum *Rep. Prog. Phys.* **84** 055901
[13] Koshelev K L, Sadrieva Z F, Shcherbakov A A, Kivshar Y S and Bogdanov A A 2023 Bound states in the continuum in photonic structures *Phys.-Usp.* **66** 494
[14] von Neumann J and Wigner E P 1929 Über merkwürdige diskrete eigenwerte *Phys. Z.* **30** 465
[15] Fairbairn W M 1968 Surface states in the linear chain with next-nearest-neighbour interactions *Surf. Sci.* **9** 439
[16] Fisher M E and Selke W 1981 Low temperature analysis of the axial next-nearest neighbour Ising model near its multiphase point *Phil. Trans. R. Soc.* A **302** 1–44
[17] Landau D P 1983 Critical and multicritical behavior in a triangular-lattice-gas Ising model: repulsive nearest-neighbor and attractive next-nearest-neighbor coupling *Phys. Rev.* B **27** 5604
[18] Han J H, Thouless D J, Hiramoto H and Kohmoto M 1994 Critical and bicritical properties of Harper's equation with next-nearest-neighbor coupling *Phys. Rev.* B **50** 11365
[19] Chandler C J, Prosko C and Marsiglio F 2016 The effect of next-nearest neighbour hopping in the one, two and three dimensional Holstein model *Sci. Rep.* **6** 32591
[20] Laha A, Biswas A and Ghosh S 2017 Next-nearest-neighbor resonance coupling and exceptional singularities in degenerate optical microcavities *J. Opt. Soc. Am.* B **34** 2050
[21] Leykam D, Mittal S, Hafezi M and Chong Y D 2018 Reconfigurable topological phases in next-nearest-neighbor coupled resonator lattices *Phys. Rev. Lett.* **121** 023901
[22] Chen Y, Kadic M and Wegener M 2021 Roton-like acoustical dispersion relations in 3D metamaterials *Nat. Commun.* **12** 3278
[23] Downing C A and Saroka V A 2021 Exceptional points in oligomer chains *Commun. Phys.* **4** 254
[24] Aristov D, Sigurdsson H and Lagoudakis P G 2022 Screening nearest-neighbor interactions in networks of exciton-polariton condensates through spin-orbit coupling *Phys. Rev.* B **105** 155306
[25] Wang K, Chen Y, Kadic M, Wang C and Wegener M 2022 Nonlocal interaction engineering of 2D roton-like dispersion relations in acoustic and mechanical metamaterials *Commun. Mater.* **3** 35
[26] Kazemi A, Deshmukh K J, Chen F, Liu Y, Deng B, Fu H C and Wang P 2023 Drawing dispersion curves: band structure customization via nonlocal phononic crystals *Phys. Rev. Lett.* **131** 176101
[27] Periwal A, Cooper E S, Kunkel P, Wienand J F, Davis E J and Schleier-Smith M 2021 Programmable interactions and emergent geometry in an array of atom clouds *Nature* **600** 630
[28] Zhu Z *et al* 2022 Observation of multiple rotons and multidirectional roton-like dispersion relations in acoustic metamaterials *New J. Phys.* **24** 123019
[29] Iglesias Martínez J A, Groß M F, Chen Y, Frenzel T, Laude V, Kadic M and Wegener M 2021 Experimental observation of roton-like dispersion relations in metamaterials *Sci. Adv.* **7** eabm2189
[30] Bossart A and Fleury R 2023 Extreme spatial dispersion in nonlocally resonant elastic metamaterials *Phys. Rev. Lett.* **130** 207201
[31] Alisepahi A R, Sarkar S, Sun K and Ma J 2023 Breakdown of conventional winding number calculation in one-dimensional lattices with interactions beyond nearest neighbors *Commun. Phys.* **6** 334
[32] Caselli N, Riboli F, La China F, Gerardino A, Li L, Linfield E H, Pagliano F, Fiore A, Intonti F and Gurioli M 2015 Tailoring the photon hopping by nearest-neighbor and next-nearest-neighbor interaction in photonic arrays *ACS Photonics* **2** 565
[33] Senanian A, Wright L G, Wade P F, Doyle H K and McMahon P L 2023 Programmable large-scale simulation of bosonic transport in optical synthetic frequency lattices *Nat. Phys.* **19** 1333
[34] Alyatkin S, Topfer J D, Askitopoulos A, Sigurdsson H and Lagoudakis P G 2020 Optical control of couplings in polariton condensate lattices *Phys. Rev. Lett.* **124** 207402
[35] Dovzhenko D, Aristov D, Pickup L, Sigurdsson H and Lagoudakis P G 2023 Next-nearest-neighbor coupling with spinor polariton condensates *Phys. Rev.* B **108** L161301
[36] Troyer M, Tsunetsugu H and Rice T M 1996 Properties of lightly doped $t-J$ two-leg ladders *Phys. Rev.* B **53** 251
[37] Donohue P and Giamarchi T 2001 Mott–superfluid transition in bosonic ladders *Phys. Rev.* B **63** 180508(R)
[38] Orignac E and Giamarchi T 2001 Meissner effect in a bosonic ladder *Phys. Rev.* B **64** 144515
[39] Robinson N J, Essler F H L, Jeckelmann E and Tsvelik A M 2012 Finite wave vector pairing in doped two-leg ladders *Phys. Rev.* B **85** 195103
[40] Wei R and Mueller E J 2014 Theory of bosons in two-leg ladders with large magnetic fields *Phys. Rev.* A **89** 063617
[41] Ye R, Li G, Wang L, Wu X, Yuan L and Chen X 2022 Controlling localized states in a two-leg ladder lattice with diagonal edges via gain/loss *Opt. Mater. Express* **12** 4755
[42] Atala M, Aidelsburger M, Lohse M, Barreiro J T, Paredes B and Bloch I 2014 Observation of chiral currents with ultracold atoms in bosonic ladders *Nat. Phys.* **10** 588
[43] Greschner S, Piraud M, Heidrich-Meisner F, McCulloch I P, Schollwöck U and Vekua T 2015 Spontaneous increase of magnetic flux and chiral–current reversal in bosonic ladders: swimming against the tide *Phys. Rev. Lett.* **115** 190402
[44] Tai M E, Lukin A, Rispoli M, Schittko R, Menke T, Borgnia D, Preiss P M, Grusdt F, Kaufman A M and Greiner M 2017 Microscopy of the interacting Harper-Hofstadter model in the two-body limit *Nature* **546** 519
[45] An F A, Meier E J and Gadway B 2017 Direct observation of chiral currents and magnetic reflection in atomic flux lattices *Sci. Adv.* **3** e1602685

[46] Zhu Q et al 2022 Observation of thermalization and information scrambling in a superconducting quantum processor Phys. Rev. Lett. 128 160502
[47] Li Y, Du H, Wang Y, Liang J, Xiao L, Yi W, Ma J and Jia S 2023 Observation of frustrated chiral dynamics in an interacting triangular flux ladder Nat. Commun. 14 7560
[48] Deng H, Dai H, Huang J, Qin X, Xu J, Zhong H, He C and Lee C 2015 Cluster Gutzwiller study of the Bose-Hubbard ladder: ground-state phase diagram and many-body Landau-Zener dynamics Phys. Rev. A 92 023618
[49] Qiao X, Zhang X-B, Jian Y, Zhang A-X, Yu Z-F and Xue J-K 2021 Quantum phases of interacting bosons on biased two-leg ladders with magnetic flux Phys. Rev. A 104 053323
[50] Padhan A, Parida R, Lahiri S, Giri M K and Mishra T 2023 Quantum phases of constrained bosons on a two-leg Bose-Hubbard ladder Phys. Rev. A 108 013316
[51] Fan J, Zhou X and Jia S Quantum phases of the biased two-chain-coupled Bose-Hubbard ladder (arXiv:2308.15042)
[52] Brillouin L 1953 Wave Propagation in Periodic Structures: Electric Filters and Crystal Lattices (Dover)
[53] Altland A and Zirnbauer M R 1997 Nonstandard symmetry classes in mesoscopic normal-superconducting hybrid structures Phys. Rev. B 55 1142
[54] Velasco C G and Paredes B 2019 Classification of topological ladder models (arXiv:1907.11460)
[55] Bell R J and Dean P 1970 Atomic vibrations in vitreous silica Discuss. Faraday Soc. 50 55
[56] Edwards J T and Thouless D J 1972 Electrons in disordered systems and the theory of localization J. Phys. C: Solid State Phys. 5 807
[57] Torres-Herrera E J, Méndez-Bermúdez J A and Santos L F 2019 Level repulsion and dynamics in the finite one-dimensional Anderson model Phys. Rev. E 100 022142
[58] Schiulaz M, Távora M and Santos L F 2018 From few- to many-body quantum systems Quantum Sci. Technol. 3 044006
[59] Sarkar M, Ghosh R, Sen A and Sengupta K 2021 Mobility edge and multifractality in a periodically driven Aubry-André model Phys. Rev. B 103 184309
[60] Duthie A, Roy S and Logan D E 2022 Anomalous multifractality in quantum chains with strongly correlated disorder Phys. Rev. B 106 L020201
[61] Aditya S, Sengupta K and Sen D 2023 Periodically driven model with quasiperiodic potential and staggered hopping amplitudes: engineering of mobility gaps and multifractal states Phys. Rev. B 107 035402
[62] Mehta M L 1967 Random Matrices and the Statistical Theory of Energy Levels (Academic)
[63] Guhr T, Müller-Groeling A and Weidenmüller H A 1998 Random-matrix theories in quantum physics: common concepts Phys. Rep. 299 189
[64] Oganesyan V and Huse D A 2007 Localization of interacting fermions at high temperature Phys. Rev. B 75 155111
[65] Atas Y Y, Bogomolny E, Giraud O and Roux G 2013 Distribution of the ratio of consecutive level spacings in random matrix ensembles Phys. Rev. Lett. 110 084101
[66] Cuevas E, Feigel'man M, Ioffe L and Mezard M 2012 Level statistics of disordered spin-1/2 systems and materials with localized Cooper pairs Nat. Commun. 3 1128
[67] Agarwal K, Gopalakrishnan S, Knap M, Müller M and Demler E 2015 Anomalous diffusion and Griffiths effects near the many-body localization transition Phys. Rev. Lett. 114 160401
[68] Morong W, Liu F, Becker P, Collins K S, Feng L, Kyprianidis A, Pagano G, You T, Gorshkov A V and Monroe C 2021 Observation of Stark many-body localization without disorder Nature 599 393
[69] Downing C A and Martín-Moreno L 2021 Polaritonic Tamm states induced by cavity photons Nanophotonics 10 513
[70] Zhou Z, Huang S, Li D, Zhu J and Li Y 2022 Broadband impedance modulation via non-local acoustic metamaterials Natl Sci. Rev. 9 nwab171
[71] Allard T F and Weick G 2022 Disorder-enhanced transport in a chain of lossy dipoles strongly coupled to cavity photons Phys. Rev. B 106 245424
[72] Allard T F and Weick G 2023 Multiple polaritonic edge states in a Su-Schrieffer-Heeger chain strongly coupled to a multimode cavity Phys. Rev. B 108 245417
[73] John S 1991 Localization of light Phys.Today 44 32
[74] Forn-Diaz P, Lamata L, Rico E, Kono J and Solano E 2019 Ultrastrong coupling regimes of light-matter interaction Rev. Mod. Phys. 91 025005
[75] Downing C A and Toghill A J 2022 Quantum topology in the ultrastrong coupling regime Sci. Rep. 12 11630
[76] Zurita J, Creffield C E and Platero G 2021 Topology and interactions in the photonic Creutz and Creutz-Hubbard ladders Adv. Quantum Technol. 3 1900105
[77] Martínez Azcona P and Downing C A 2021 Doublons, topology and interactions in a one-dimensional lattice Sci. Rep. 11 12540
[78] Tarquini E, Biroli G and Tarzia M 2017 Critical properties of the Anderson localization transition and the high-dimensional limit Phys. Rev. B 95 094204
[79] Zimmermann T, Köppel H, Haller E, Meyer H-D and Cederbaum L S 1987 Energy level statistics of coupled oscillators Phys. Scr. 35 125
[80] Pandey A and Ramaswamy R 1991 Level spacings for harmonic-oscillator systems Phys. Rev. A 43 4237
[81] Chakrabarti B and Hu B 2003 Level correlation in coupled harmonic oscillator systems Phys. Lett. A 315 93-100